ACS APPLIED MATERIALS & INTERFACES

www.acsami.org Review

A Critical Review of Thermal Boundary Conductance across Wide and Ultrawide Bandgap Semiconductor Interfaces

Tianli Feng,* Hao Zhou, Zhe Cheng, Leighann Sarah Larkin, and Mahesh R. Neupane

Cite This: *ACS Appl. Mater. Interfaces* 2023, 15, 29655−29673 Read Online

ACCESS | Metrics & More | Article Recommendations

ABSTRACT: The emergence of wide and ultrawide bandgap semiconductors has revolutionized the advancement of next-generation power, radio frequency, and opto- electronics, paving the way for chargers, renewable energy inverters, 5G base stations, satellite communications, radars, and light-emitting diodes. However, the thermal boundary resistance at semiconductor interfaces accounts for a large portion of the near-junction thermal resistance, impeding heat dissipation and becoming a bottleneck in the devices' development. Over the past two decades, many new ultrahigh thermal conductivity materials have emerged as potential substrates, and numerous novel growth, integration, and characterization techniques have emerged to improve the TBC, holding great promise for efficient cooling. At the same time, numerous simulation methods have been developed to advance the understanding and prediction of TBC. Despite these advancements, the existing literature reports are widely dispersed, presenting varying TBC results even on the same heterostructure, and there is a large gap between experiments and simulations. Herein, we comprehensively review the various experimental and simulation works that reported TBCs of wide and ultrawide bandgap semiconductor heterostructures, aiming to build a structure−property relationship between TBCs and interfacial nanostructures and to further boost the TBCs. The advantages and disadvantages of various experimental and theoretical methods are summarized. Future directions for experimental and theoretical research are proposed.

KEYWORDS: *ultrawide bandgap semiconductors, heterostructures, nanostructures, thermal boundary conductance, phonons*

1. INTRODUCTION

Wide and ultrawide band gap semiconductors (WBGSs and UWBGSs) have gained renewed and fast-growing interest,[1] driven by the great potential in new technologies such as power electronics (e.g., computer/phone chargers, inverters for renewable energy grid and electric vehicles, power supply), radio frequency (RF) electronics (e.g., wireless communications like 5G base station, satellite communications, radars), and optoelectronics (e.g., light-emitting diodes) as shown in Figure 1. Good thermal management is essential for these devices to prevent or minimize severe self-heating effects[2] and maintain stability and reliability.[2−6] As electronic devices continue to push the boundaries of power density and size, reducing thermal boundary resistance (TBR) at the interfaces between the active material and substrate,[7−14] which has a substantial contribution to the near-junction thermal resistance, has become increasingly important.[15−17]

Gallium nitride (GaN) and beta-phase gallium oxide (β-Ga_2O_3) are the two most promising WBGS and UWBGS that are being studied extensively nowadays. GaN transistors can be operated with lower switching losses, higher frequency, and higher power density[18] compared to conventional Si-based transistors. β-Ga_2O_3 is an emerging UWBGS for the next-generation power devices owing to its ultrawide bandgap of 4.8 eV and a corresponding high breakdown field of 8 MV cm^{-1}.[19−22] Aside from bandgap, thermal conductivity is also an important factor to consider in order to operate at high power. Figure 2 summarizes the bandgaps and thermal conductivities of materials that are present in WBGS and UWBGS heterostructures. Among them, Si and Ge are the first-generation semiconductors with bandgaps of 1.12 and 0.66 eV, respectively. Wide bandgap semiconductors include GaN (3.4 eV) and SiC (3.26 eV). Ultrawide bandgap semiconductors include β-Ga_2O_3 (4.8 eV), diamond (5.47 eV), AlN (6.23 eV), and AlGaN (3.4−6.23 eV). β-Ga_2O_3 attracted great attention since 2012 because of the advancement in growth technique[22,23], which enables large-diameter, potentially low-

Received: February 21, 2023
Accepted: May 29, 2023
Published: June 16, 2023

Downloaded via UNIV OF UTAH on June 25, 2024 at 16:03:58 (UTC).
See https://pubs.acs.org/sharingguidelines for options on how to legitimately share published articles.

ACS Publications © 2023 American Chemical Society

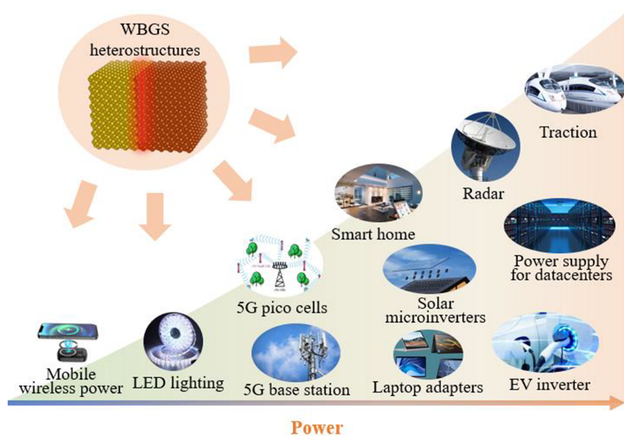

Figure 1. Applications of WBGSs in future technologies where thermal management is crucial.

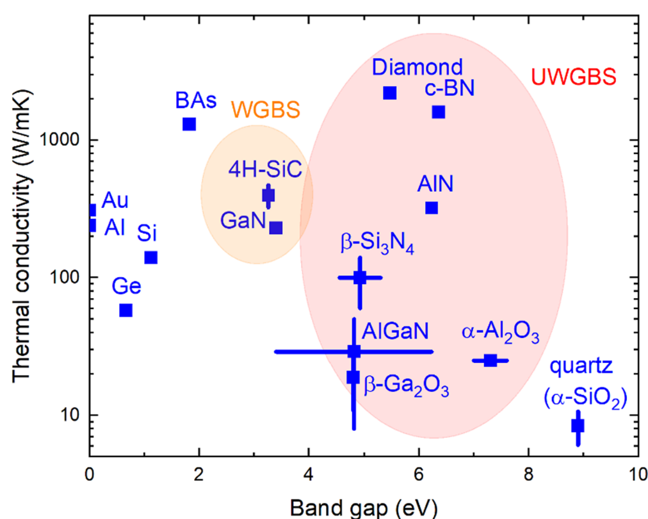

Figure 2. Bandgaps and room-temperature bulk thermal conductivities of materials that are present in WBGS and UWBGS heterostructures. Relevant references: Si,[35,36] Ge,[36] (wurtzite type) GaN,[37] 4H-SiC,[38] β-Ga_2O_3,[39] diamond,[40,41] (wurtzite type) AlN,[42] AlGaN,[43−47] c-BN,[48] Si_3N_4,[49] (cubic) BAs,[50] and SiO_2.[51]

cost, and high-quality wafers grown from the melt. The broad-scale application of β-Ga_2O_3 is limited by its low thermal conductivity and the difficulty of p-type doping.[24] Diamond is considered the ultimate UWBGS as it has the highest thermal conductivity in nature, high breakdown field, high mobility, and high saturation velocity.[25] However, the application of diamond is limited by the available wafer size (up to 1.5 in. for now) and n-type doping. AlN has excellent bandgap and thermal conductivity and is now very promising among UWBGSs due to a recent advancement.[26] Figure 2 also lists important substrates including metals, quartz (SiO_2), and sapphire (Al_2O_3). Aluminum (Al) and gold are widely used for electrical contacts in device fabrications,[27] and SiO_2 is typically used near the gates of dielectrics.[28] For better thermal management, high-thermal-conductivity materials such as SiC and diamond can be used as the substrate. More recently, the growth of AlN has reached a maturity, making it another promising substrate candidate.[29−34]

However, the interface between active materials and substrates shows undesired high thermal resistance and impedes heat dissipation in these electronic devices. To improve the thermal boundary conductance (TBC), many advanced experimental techniques have been developed to enable the covalent bonding of many materials with atomic-level clean contact, which in turn has improved the TBCs significantly. These numerous papers reported various interfacial structures including a third intermediate layer, an amorphous interfacial region, defects, and disorder, which result in various TBC values even for the same heterostructures. They also lack theoretical guidance on how to select the interlayer materials and design the interface structure such as the thickness of the interlayer, geometry of teeth, degree of disorder, and concentration of defects. Therefore, there is an urgency to review the experimental and theoretical works, figure out the gaps, and point out the directions.

In this article, we review the recent progress of the TBC enhancement for WBGS and UWBGS heterostructures and point out future research directions. The review is organized as follows: In Section 2, we briefly review the distinct importance of thermal boundary conductance in overall thermal management for WBGS and UWBGS devices. In Section 3, we recap the start-of-the-art understanding of thermal transport mechanisms across interfaces and the impacts of various nanostructures. In Section 4, we briefly summarize the recent advances in experimental growth and joining technologies as well as TBC simulation methods. In Section 5, we summarize in detail all the experimental and simulation TBC data for GaN/diamond,[52,53] GaN/Si,[54] GaN/SiC,[55] GaN/AlN,[56] GaN/oxides,[57] GaN/metals,[58] Si/diamond,[59] Si/SiC, β-Ga_2O_3/diamond,[60] β-Ga_2O_3/SiC,[61] and β-Ga_2O_3/metals interfaces to date. We extract the details of the interfacial nanostructures in order to build a structure−property relationship, which helps us understand the underlying mechanisms for the TBC improvement for each interface. In Sections 6 and 7, a summary together with possible strategies to improve TBC and future research directions are proposed for specific interfaces.

2. ROLE OF TBC IN (U)WBGS DEVICE THERMAL MANAGEMENT

Wide and ultrawide bandgap semiconductors-based electronics generate localized hot spots with a size of tens of nanometers near the gate where a large electric field drop exists during operation.[7−14] The peak temperature of the hot spots limits the device's performance and reliability.[24] Most of the near-junction thermal management strategies aim to lower the peak temperature by spreading the heat, to either the upper side through the gate metal or the lower side through the substrate.[62] Before that, the localized heat must flow through the semiconductor-metal interfaces and semiconductor-substrate interfaces.[63] That poses a critical role of TBC in these electronics. For example, a GaN-diamond TBC of 50 MW m^{-2} K^{-1} is equivalent to the thermal resistance of 4 μm GaN or 44 μm diamond. A Ga_2O_3-SiC TBC of 50 MW m^{-2} K^{-1} is equivalent to the thermal resistance of 300 nm Ga_2O_3 or 9 μm SiC. The GaN or Ga_2O_3 layer thickness in the devices is a balance of materials saving, thermal consideration, and electric field blocking. It is desired to put diamond and SiC as close as possible to the hot spots in order to save GaN or $_2O_3$ materials and make the GaN or Ga_2O_3 layer as thin as possible. However, thin GaN or Ga_2O_3 layers cannot block the large electric field due to dislocations and defects in GaN or Ga_2O_3 and along the GaN or Ga_2O_3 -substrate interfaces. Therefore, the active GaN or Ga_2O_3 layer in the device is typically on the

https://doi.org/10.1021/acsami.3c02507
ACS Appl. Mater. Interfaces 2023, 15, 29655−29673

order of 1 or 2 μm. In this scenario, the metal–semiconductor TBC is comparably important for both β-Ga_2O_3 and GaN electronics; the effect of semiconductor-substrate TBC on β-Ga_2O_3 electronics is much less important than GaN electronics because of the low thermal conductivity of β-Ga_2O_3. However, it is much easier to grow high-quality β-Ga_2O_3 than GaN. Therefore, it is possible to use a much thinner drift layer in β-Ga_2O_3 electronics in the future than GaN electronics. Then, the TBC of the β-Ga_2O_3-substrate interface becomes important as well. For example, Wang and Zhou[64] show that for a 100 nm β-Ga_2O_3 on 100 μm AlN heterostructure, the maximum temperature can be decreased by 38% when the TBC increased from 10 to 310 MW m^{-2} K^{-1} under a power 10.1 GW m^{-2}.

The above discussion focuses on near-junction cooling. After heat spreading, the generated heat flows through the substrate and thermal interface material, and finally dissipates into the heat sink. The typical substrate thickness is 200 μm. Nowadays backside polishing technique can reduce the substrate thickness down to about 50 μm with additional cost. Thinner substrates contribute to better heat dissipation while the extra expense limits its wide adoption. In most cases, the thermal resistances from the substrate and the thermal interface materials are much larger than the thermal resistances of the gate metal–semiconductor and semiconductor-substrate interfaces. Therefore, increasing the TBC discussed in this review contributes to lowering the peak local temperature but is not significantly helpful to lower the overall average temperature of the devices. To lower the average temperature of the devices, additional cooling strategies in the level of the device package are needed, which are not the focus of this review. Device level calculations of the effect of the semiconductor-substrate TBC on the peak temperature of the devices can be found elsewhere.[7−14,64−68]

3. INTERFACIAL PHONON TRANSPORT MECHANISMS AND IMPACTS OF INTERFACIAL STRUCTURES

Before diving into specific semiconductor interfaces, it is necessary to review the current state-of-the-art understanding of general interfacial thermal transport, in order to understand the TBC values. Based on the review articles by Hopkins,[69] Monachon, Weber, and Dames,[70] Giri and Hopkins,[71] and Chen et al.,[72] TBC depends on two factors, i.e., (a) the intrinsic properties of the two materials comprising the interface or irradiance of heat carriers bombarding an interface and (b) the extrinsic impacts of the interfacial structure that affect transmission coefficients, such as intermediate layers, interlaced teeth, interfacial atomic mixing, and atomic impurities and defects. The intrinsic properties cannot be tuned for a given interface, and thus, we focus on the discussion of extrinsic impacts on transmission in this article.

As shown in Figure 3, when a phonon approaches an interface,[73] the transmission can happen either elastically (preserving frequency) or inelastically (varying frequency), affected by phonon density of states (DOS) overlap, lattice anharmonicity, interface defects and disorder, intermediate material, interface bonding strength, etc. However, these impacts are strongly materials dependent, i.e., the same interfacial structure can increase or decrease the TBC. For example, the compositional intermixing at the interface was found to decrease the TBC for Cr/Si system,[69] but was found to increase the TBC for Si/Ge system.[74,75] The interface

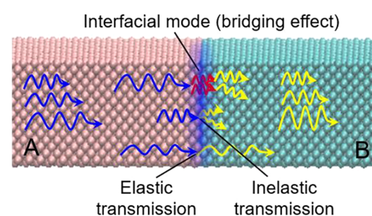

Figure 3. Summary of phonon transmission mechanism across an interface.

geometric roughness was found to decrease TBC for the Al/Si system but increase TBC for the Si/diamond[76] and Si/SiC system.[77] Many other examples can be found in ref 73. This makes the guidance from the previous review articles based on different systems limited when being applied to the systems discussed in this article.

The possible impacts of the interfacial nanostructures on TBC are summarized[73] in Figure 4. Each interfacial structure

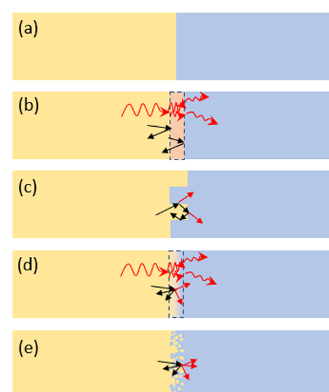

Figure 4. Summary of impacts of interfacial structures on TBC. (a) Bare interface. (b) The addition of an interlayer can bridge phonon spectra but will introduce one more interface. (c) Adding interlaced teeth may improve transmission or reflection. (d,e) Interfacial mixing and defects may enhance the inelastic transmission or reflection.

can have two competing effects on phonon transmissions—one tends to increase phonon transmission while the other tends to decrease phonon transmission. As a result, each type of interfacial structure can either increase or decrease the TBCs, depending on the properties of the bulk materials comprising the interface and the detailed interfacial structures.[73] For example, with the addition of an intermediate layer, the phonon vibrational bridging effect can increase the phonon transmission, but at the same time, the interlayer introduces an extra interface which can reflect phonons. Similarly, the introduction of interlaced teeth can increase the contact area and increase phonon transmission, but at the same time, the larger contact area can increase phonon defection and reflection.[77] The various TBC values reported in different works for the same interface, as will be discussed in the following sections, are mainly due to the various interfacial nanostructures as shown in Figure 4.

4. SUMMARY OF EXPERIMENTAL AND SIMULATION METHODS

Over the past decades, many advanced growth and bonding techniques have been employed or developed for creating high-quality WBGS and UWBGS heterostructures. The

https://doi.org/10.1021/acsami.3c02507
ACS Appl. Mater. Interfaces 2023, 15, 29655−29673

Table 1. Summary of Experimental Methods for Growing (U)WBGS Heterointerfaces and Simulation Methods for Predicting TBCs

Growth/Bonding Method		Advantages	Disadvantages	
Deposition methods (layer-by-layer growth)	MBE	Very clean interface	Expensive and slow	
	ALD	Good-quality interface	Expensive and slow	
	CVD	Cheaper and simpler than MBE	Need high temperatures; form an interlayer due to chemical reaction; less controllable than MBE	
	MOCVD	Relatively efficient than MBE; high-quality interface	Need high temperatures; often hazardous and toxic; expensive; less controllable than MBE	
Bonding methods (bond two grown materials)	Plasma bonding	Can bond most materials by using an intermediate oxide material	Results in an oxide interlayer, which needs high T annealing to remove oxide and strengthen the bonding	
	Hydrophobic bonding	Can form strong chemical bonds	Results in a (non-uniform) interlayer	
	Hydrophilic bonding	Can form strong chemical bonds	Results in a (uniform) interlayer interface de-bond at higher temperatures	
	SAB	Can be done at room temperature and form strong covalent bonds	Form an amorphous interlayer in between, which needs high-T annealing to turn into crystalline	
Landauer's formula, or Monte Carlo	AMM, DMM	Simple No need simulations	• No inelastic • No interfacial bonding information • No heterostructure geometry information	No interfacial phonon modes; No phonon local nonequilibrium; No size effect
	AGF (harmonic)	Accurate for elastic transmission	• No inelastic • Simple interface geometry	
	AGF (anharmonic)	Can capture inelastic transmission	• Simple interface geometry	
	Wave packet	Can extract transmission of the individual phonon mode	• 0 K – other phonons freeze out • Slow – one mode at a time • Depends on the quality of interatomic potential	
NEMD	Transmission coefficient not needed	Captures all natural phonon interfacial phenomena	• Unavailability of suitable empirical interatomic potentials for most heterostructures • No direct physical insights into mode-dependent phonon transmission information • Requires quantum corrections at low temperatures	

methods together with their advantages and disadvantages are summarized in Table 1. They include molecular beam epitaxy (MBE),[78−81] atomic layer deposition (ALD),[82] physical vapor deposition (PVD)[83] chemical vapor deposition (CVD),[4,79,84,85−98] metal−organic chemical vapor deposition (MOCVD),[78,99,100] plasma bonding,[101] and very recently developed nanoscale graphoepitaxy,[76] hydrophobic bonding,[102] hydrophilic bonding,[102,103] and room-temperature (RT) surface-activated bonding (SAB).[61,82,104−107] These advanced technologies have successfully integrated GaN and Ga_2O_3 with single crystal diamond.[52,66,82−84,85−92,99,104,105,108,109] Figure 5 shows some examples of the interfaces formed by advanced growth or bonding technologies. It is seen that all have close atomic contact without voids or gaps. Most heterostructures have intermediate transition layers, namely, interlayers, which can tightly bond the two materials. The thickness of the interlayer can be as small as a few nanometers, which can have a minimal increase in thermal resistance and at the same time can bridge the phonon spectra of the two sides. The interface quality, nanomorphology, and interlayer materials can be well characterized, providing important details for theoretical analysis. Among the methods, the most notable one is the newly developed RT-SAB, which is not restricted by crystal growth methods and can chemically bond two grown materials at room temperature. This method also often leaves a third intermediate amorphous layer at the interface, which can be reduced and even eliminated by annealing.

Advanced measurement methods have also been developed to measure the TBCs such as time-domain thermoreflectance (TDTR),[110] frequency-domain thermoreflectance (FDTR),[111] optical transient interferometric mapping (TIM),[112] contactless thermoreflectance (CTR),[52] and transient thermoreflectance (TTR).[84,86,90,99,102,113,114] These experimental advances have significantly improved the accuracy of the TBC data and provided opportunities to push the boundaries of cutting-edge high-energy density applications.

Recent years have also seen rapid progress in the development of numerical, analytical, and atomistic methods to understand and predict phonon thermal transport across heterostructures. Comprehensive reviews can be found in refs 69−72. As shown in Table 1, these methods can be divided into two categories. The first category includes Landauer's formula and Monte Carlo simulations, which require phonon transmission coefficients as input. The second category is molecular dynamics (MD), especially nonequilibrium MD (NEMD), which does not require phonon transmission coefficients as input. To calculate phonon transmission coefficients, common ways are acoustic mismatch (AMM),[115] diffuse mismatch (DMM),[116,117] and atomic Green's function (AGF).[75,118−120] These methods, however, assume elastic phonon transport and neglect the inelastic part.

https://doi.org/10.1021/acsami.3c02507
ACS Appl. Mater. Interfaces 2023, 15, 29655−29673

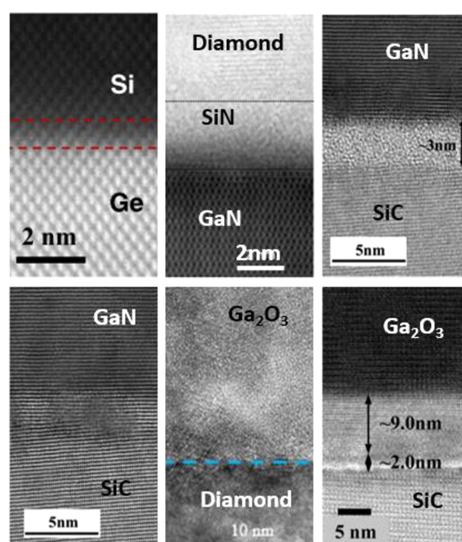

Figure 5. High-resolution TEM images of state-of-the-art interfaces for Si/Ge,[74] GaN/diamond,[85] GaN/SiC,[106] Ga_2O_3/diamond,[82] and Ga_2O_3/SiC.[61] Reprinted in part with permission from refs 74, 85, 106, 82, and 61. Copyright 2021 The Author(s). Copyright 2018 American Chemical Society. Copyright 2019 American Chemical Society. Copyright 2020 American Institute of Physics. Copyright 2020 American Chemical Society.

Although some works[121−129] have improved these methods to incorporate the inelastic contribution, they cannot include other important phenomena such as the existence of interfacial phonon modes and the local phonon nonequilibrium. The wave packet method[130−134] is an effective way to study phonon transmission, but it can only study one mode at a time, which is time-consuming. More importantly, it must be performed at 0 K, assuming all the other modes are frozen out, which misses the phonon−phonon coupling effect at finite temperatures. Compared to the above-mentioned methods based on phonon transmission coefficients, MD is the best one which can naturally include all the physical phenomena near the interfaces. MD has two intrinsic limitations: it severely depends on interatomic potentials, which are nonexistent for most heterostructures (and may not be accurate if they exist); it does not explicitly provide phonon transmission information. The first limitation can be partly solved by machine learning. Cheng et al. developed machine learning interatomic potential for Si/Ge interface trained from DFT calculations and yielded excellent results that agree well with experimental data.[74] The second limitation can be partly mitigated by various spectral phonon analysis methods.[135−144]

5. TBCS OF (U)WBGS HETEROSTRUCTURES

5.1. GaN/Diamond Interface. Single crystal diamond has the highest thermal conductivity of ∼2200 W m^{-1} K^{-1} and is naturally considered the ideal candidate for the substrate of wide bandgap electronics. The first reported TBC between GaN and diamond is <10 MW m^{-2} K^{-1} by Kuzmik et al.[145] in 2011 for an MBE-grown GaN on a single crystalline diamond measured by the TIM technique. But they did not assess the quality of the GaN buffer or interface, and their measurement method is considered to have a large uncertainty. In 2013, Cho et al. reported a much larger TBC of about 21−28 MW m^{-2} K^{-1} for a high-temperature bonded GaN/diamond interface measured by using TDTR, a much more accurate method.[108] An adhesion layer was found between GaN and diamond, but no more details were provided for the adhesion layer. Right after that, Pomeroy et al. increased the TBC further to 37 MW m^{-2} K^{-1} for a CVD-grown interface, in which a ∼25 nm-thick dielectric layer was found between GaN and diamond.[146] As a comparison, another sample with a ∼50 nm-thick dielectric layer at the interface showed a TBC of only 28 MW m^{-2} K^{-190}, indicating that a thinner interlayer at the interface is better for interfacial thermal transport. After that, many works have strived to improve the quality of the interface and reduce the interlayer thickness by the CVD and MOCVD growth methods. Significant success has been achieved, as listed in Table 2.

The minimum interlayer thickness obtained to date for GaN/diamond interface is ∼5 nm. The interlayers such as SiN_x and AlN are deposited on GaN as protective layers first before growing nanocrystalline diamond by CVD because the plasma during CVD growth can etch GaN. The large roughness of the CVD-grown nanocrystalline diamond affects thermal measurements by optical techniques such as TDTR and TTR. Samples with multiple layers have multiple unknown parameters in data fitting, which are difficult to separate. The large roughness and unknown fitting parameters contribute to the large error bars in measuring these CVD diamonds grown on GaN samples. The largest value reported to date is 167−400 MW m^{-2} K^{-1} by Gu et al. in 2016[52] and 323 MW m^{-2} K^{-1} by Malakoutian et al. in 2021.[99] Both have a ∼5 nm SiN_x interlayer. However, these relatively high values may need reinvestigation because the ∼5 nm SiN_x interlayer alone can provide more resistance than the reported total thermal boundary resistance. The thermal resistance of a 5 nm amorphous SiN_x layer is about 5 nm/(1 W m^{-1} K^{-1}) = 5 m^2 K GW^{-1}, which corresponds to a TBC of 200 MW m^{-2} K^{-1}. Even if the thermal resistances of the two interfaces (GaN-SiN_x and SiN_x-diamond) are zero, the TBC cannot exceed 200 MW m^{-2} K^{-1}. Even if the SiN_x interlayer is partially crystalline, its thermal conductivity cannot be high due to the strong size effect (∼5 nm). We hypothesize that the high TBC values might originate from the arbitrariness during their fitting process, which contains too many unknown parameters (six thermal conductivity values and five TBC values given that their samples have six layers). In comparison, the ∼5 nm AlN interlayer gives about 55−100 MW m^{-2} K^{-1} by Gu et al. in 2016[52] and Yates et al. in 2018.[85] We are unable to conclude that SiN_x is better than AlN as the interlayer because the TBC depends largely on the quality of the interlayer as well.

Besides CVD, Cheng et al.[104] and Mu et al.[105] have demonstrated the SAB method that can bond GaN with the diamond at room temperature. After SAB, an interlayer made of amorphous Si (a-Si) and amorphous diamond (a-diamond) is left between GaN and diamond. A subsequent high-temperature annealing process can turn the amorphous layer into crystalline, which can further improve the TBC. Amorphous materials typically have much lower thermal conductivity than their crystalline counterparts. The measured TBC is found to increase with decreasing interlayer (a-Si + a-diamond) thickness. The minimum interlayer obtained is 2 nm a-Si + 2.2 nm a-diamond, giving a TBC as high as 92 MW m^{-2} K^{-1} in ref 104. This value can be possibly further increased after subsequent high-temperature annealing to promote the crystalline phases. Applying the SAB method to achieve high TBC is new, and we expect more work will be done in the coming years with thinner and annealed interlayer for GaN/

Table 2. Thermal Boundary Conductance between GaN and Other Materials[a]

	Growth Method	Interlayer	Measurement Method	TBC (MW m^{-2} K^{-1})	Ref.
GaN/diamond	CVD	None	TTR	4.5	Waller 2020 [84]
GaN/diamond	CVD	None	CTR	12–15	Gu 2016 [85]
GaN/diamond	CVD	None	TDTR	21.2	Yates 2018 [86]
GaN/diamond	MBE	Unknown	Optical	<10	Kuzmik 2011 [146]
GaN/diamond	High-T bonding	Adhesion layer	TDTR	21–28	Cho 2013 [109]
GaN/diamond	RT SAB	2nm a-Si+2.2nm a-dia	TDTR	92	Cheng 2020 [105]
GaN/diamond	CVD	~5 nm AlN	CTR	55–100	Gu 2016 [85]
GaN/diamond	CVD	~5 nm SiN_x	TDTR	~100	Yates 2018 [86]
GaN/diamond	CVD	~5 nm SiN_x	TTR	~150	Zhou 2017 [4,87]
GaN/diamond	CVD	~5 nm SiN	CTR	167–400*	Gu 2016 [85]
GaN/diamond	MOCVD	~5 nm SiN_x	TTR	323*	Malakoutian 2021 [100]
GaN/diamond	CVD	~5 nm AlN	TDTR	55	Yates 2018 [86]
GaN/diamond	SAB	10nm a-Si+3nm a-dia	TDTR	53	Cheng 2020 [105]
GaN/diamond	SAB+800°C ann.	15nm c-Si+3nm a-dia	TDTR	70	Mu 2021 [106]
GaN/diamond	SAB	15nm a-Si+3nm a-dia	TDTR	30	Mu 2021 [106]
GaN/diamond	SAB	22nm a-Si+3nm a-dia	TDTR	25	Mu 2021 [106]
GaN/diamond	SAB+800°C ann.	24nm c-Si+3nm a-dia	TDTR	85	Mu 2021 [106]
GaN/diamond	High-T bonding	~22 nm SiN_x	TDTR	51–57	Cho 2017 [110]
GaN/diamond	CVD	~25 nm SiN_x	TDTR	~35	Cho 2014 [88]
GaN/diamond	CVD	~25 nm dielectric	Raman	~37	Pomeroy 2013 [147], 2014 [90]
GaN/diamond	CVD	28 nm SiN_x	TTR	83	Sun 2015 [91]
GaN/diamond	High-T bonding	~31 nm SiN	TDTR	31	Cho 2017 [110]
GaN/diamond	CVD	~40 nm dielectric	Raman	34.5	Altman 2014 [92]
GaN/diamond	CVD	~50 nm dielectric	Raman	56	Dumka 2013 [93]
GaN/diamond	PVD	Ti (5 nm)/AuSn (40 nm)/Ti (5 nm)	TDTR	13.2	Yang 2021 [83]
GaN/diamond	CVD	~50 nm dielectric	Raman	~28	Pomeroy 2014 [90]
GaN/diamond	Simulations	None	NEMD Tersoff	~13	Tao 2017 [148]
GaN/diamond	Simulations	Monolayer graphene	NEMD Tersoff	~15	Tao 2017 [148]
GaN/diamond	Simulations	Trilayer graphene	NEMD Tersoff	~4	Tao 2017 [148]
GaN/diamond	Simulations	Interlaced teeth	NEMD Tersoff	~19	Tao 2017 [148]
GaN/diamond	Simulations	Interlaced teeth w/ monolayer graphene	NEMD Tersoff	~29	Tao 2017 [148]
GaN/diamond	Simulations	Interlaced teeth w/ trilayer graphene	NEMD Tersoff	~14	Tao 2017 [148]
GaN/diamond	AMM	N/A	Theory	~333	Cho 2017 [110]
GaN/SiC	MBE	None	FDTR	230	Ziade 2015 [80]
GaN/SiC	SAB	3 nm a-SiC	TDTR	170	Mu 2019 [107]
GaN/SiC	SAB+1000°C ann.	3 nm c-SiC (inhomo.)	TDTR	230	Mu 2019 [107]
GaN/SiC	CVD	5nm SiN	TTR	154	Zhou 2017 [87]
GaN/SiC	MOCVD	36 nm AlN	TDTR	200	Cho 2012 [78,149]
GaN/SiC	MBE	38 nm AlN	TDTR	185	Cho 2014 [88]
GaN/SiC	Epitaxial growth	50 nm AlN	TTR	40	Liu 2019 [114]
GaN/SiC	PVD	Ti (5 nm)/AuSn (40 nm)/Ti (5 nm)	TDTR	14.8	Yang 2021 [83]
GaN/SiC	MOCVD	Unknown	TIM	8.3	Kuzmík 2007 [150]
GaN/SiC	Simulations	None	NEMD Tersoff	~520	Hu 2011 [151]
GaN/SiC	Simulations	None	NEMD Tersoff	420	Hu 2013 [152]
GaN/SiC	Simulations	None	NEMD Tersoff	470	Lee 2016 [153]
GaN/SiC	Simulations	None	NEMD Tersoff	794	Lee 2017 [154]
GaN/SiC	Simulations	None	NEMD Tersoff	495	Li 2019 [155]
GaN/SiC	Simulations	None	NEMD Tersoff	470	Lee 2018 [156]
GaN/SiC	Simulations	4 nm $Ga^{15}N$ (isotope)	NEMD Tersoff	555	Lee 2018 [156]
GaN/SiC	Simulations	1×8 nm interlaced teeth	NEMD Tersoff	~800	Hu 2011 [151]
GaN/SiC	Simulations	1 nm AlN	NEMD Tersoff	570–630	Hu 2011 [151]
GaN/SiC	Simulations	Graphene	NEMD Tersoff	601	Hu 2013 [152]
GaN/SiC	Simulations	1×5-8 nm teeth	NEMD Tersoff	670	Lee 2016 [153]
GaN/SiC	Simulations	2.6 nm AB (m_A=51.7, m_B=10.3)	NEMD Tersoff	971	Lee 2017 [154]
GaN/SiC	Simulations	2.5 nm 10% boron dop.	NEMD Tersoff	716	Li 2019 [155]
GaN/SiC	Simulations	2.5 nm 50% boron allo.	NEMD Tersoff	755	Li 2019 [155]
GaN/SiC	Simulations	2.5 nm 10% boron allo.	NEMD Tersoff	577	Li 2019 [155]
GaN/Si	MBE	38 nm AlN	TDTR	188*	Cho 2012 [78]
GaN/Si	MBE	38 nm AlN	TDTR	128	Cho 2014 [79]
GaN/Si	MOCVD	100 nm AlN	TDTR	263	Yates 2015 [101]
GaN/Si	PVD	Ti (5 nm)/AuSn (40 nm)/Ti (5 nm)	TDTR	16.5	Yang 2021 [83]
GaN/AlN	MBE	None	TDTR	620	David 2009 [157]
GaN/AlN	Simulations	None	EMD/NEMD (SW) extplt. to ∞	~1150–1300	Liang 2014 [158,159]
GaN/AlN	Simulations	None	NEMD (Tersoff)	475	Lee 2018 [156]
GaN/AlN	Simulations	None	Green's function	300	Polanco 2019 [160]
GaN/AlN	Simulations	None	NEMD SW ex. ∞	825	Wang 2021 [161]
GaN/AlN	Simulations	None	NEMD LJ	780	Bao 2022 [162]
GaN/AlN	Simulations	None	Monte Carlo	870	Bao 2022 [162]
GaN/AlN	Simulations	None	NEMD SW	937	Sun 2021 [163]
GaN/AlN	Simulations	None	NEMD (Tersoff – mixing rule)	3124	Sun 2021 [163]
GaN/AlN	Simulations	None	NEMD (Transf. Tersoff)	3225	Sun 2021 [163]
GaN/AlN	Simulations	2 nm amorphous layer	NEMD SW	149	Wang 2021 [161]
GaN/AlN	Simulations	2 nm ann. cryst. layer	NEMD SW	197	Wang 2021 [161]
GaN/AlN	Simulations	Dislocation (lat. mis.)	NEMD SW	496	Sun 2021 [163]
GaN/AlN	Simulations	Dislocation (lat. mis.)	NEMD (Tersoff – mixing rule)	2440	Sun 2021 [163]
GaN/AlN	Simulations	Dislocation (lat. mis.)	NEMD (Transf. Tersoff)	1933	Sun 2021 [163]
GaN/BAs	Oxygen plasma	2-nm amorphous Al_2O_3	TDTR	250	Kang 2021 [102]
GaN/Al_2O_3	MOCVD	Unclear	TDTR	10	Wang 2014 [164]
GaN/Al_2O_3	MOCVD	Unclear	TIM	8.3	Kuzmík 2007 [150]
GaN/Al_2O_3	MOCVD	Unclear	3ω method	10	Wang 2015 [165]
GaN/SiO_2	Plasma-enh. CVD	Unclear	3ω method	15	Wang 2015 [165]
GaN/ZnO	PVD	10–12 nm defective	TDTR	490	Gaskins 2018 [166]
GaN/ZnO	Model	None	DMM	240	Gaskins 2018 [166]
GaN/ZnO	Simulations	None	AGF DFT	295	Gaskins 2018 [166]
GaN/Al	PVD	Unclear	TTR	190	Stevens 2005 [115]
GaN/Al	PVD	Unclear	TDTR	92	Donovan 2014 [12]
GaN/Al	PVD	Unclear	TDTR	160	Wang 2014 [164]
GaN/Al	PVD	Unclear	TDTR	47–161	Cho 2014 [79]
GaN/Al	PVD	Unclear	TDTR	400	Koh 2021 [81]
GaN/Au	PVD	Unclear	TDTR	55	Donovan 2014 [12]
GaN/Au	PVD	Ti adhesion layer	TDTR	~250	Donovan 2014 [12]
GaN/Cr	PVD	Unclear	TTR	230	Stevens 2005 [115]
GaN/Au or Cr	PVD	Unclear	FDTR	180	Freedman 2013 [167]
GaN/Al	Simulations	None	NEMD LJ	211	Jones 2013 [168]
GaN/Al	Simulations	Al-Ga contact	NEMD SW	99	Zhou 2013 [169]
GaN/Al	Simulations	3×7 nm Al-Ga teeth	NEMD SW	102	Zhou 2013 [169]
GaN/Al	Simulations	3×7 nm Al-N teeth	NEMD SW	172	Zhou 2013 [169]
GaN/Al	NE Landauer	None	DFT	427	Koh 2021 [81]

[a]Greened and greyed boxes are for experimental and simulation data, respectively. *These values may have a large uncertainty.

diamond interface or directly bonded GaN-diamond interface without interfacial layers, and further increased TBC is expected.

In Figure 6, we have summarized the TBC with respect to the thickness of the interlayer, from which the general trend that TBC increases with decreasing thickness can be found. Adding SiN_x or AlN between GaN and diamond can (i) enhance the transmission by strengthening the chemical bonding, (ii) increase transmission by the phonon bridging effect, and (iii) decrease the transmission by introducing one more interface. Diamond and GaN have a large phonon spectra mismatch, especially for the acoustic phonons since diamond's acoustic phonon frequency range is more than three times that of GaN. This gap is bridged by SiN_x and AlN, whose acoustic phonon frequency range is half of that of diamond. If a material with a closer acoustic phonon frequency range to diamond can be found, it will have the potential to further increase the TBC.

Despite the significant advances in the experiment, the progress of GaN/diamond TBC simulations has lagged. To date, besides the traditional AMM and DMM models, which cannot include inelastic scattering and thus are inaccurate, the only atomic level simulation was done by Tao et al. in 2017[147] with NEMD simulations. The TBC obtained is ~13 MW m^{-2} K^{-1}. Although it locates inside the range measured for bare GaN/diamond interface without an interlayer, the match is more likely a coincidence because experimental sample has a

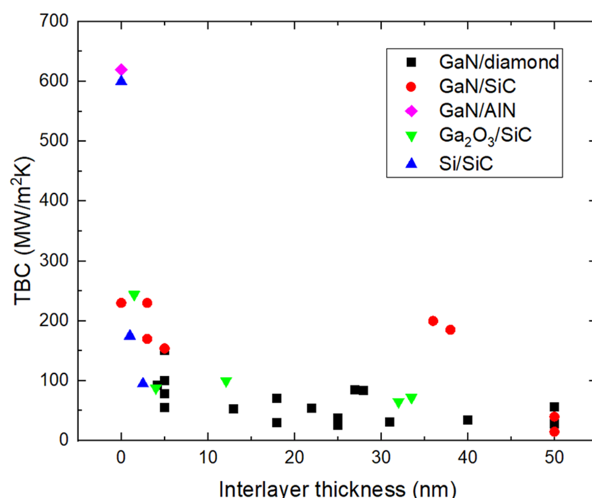

Figure 6. TBC with respect to the thickness of interlayer for various interfaces. Only the data with clear interlayer information are included.

https://doi.org/10.1021/acsami.3c02507
ACS Appl. Mater. Interfaces 2023, 15, 29655−29673

bad quality of the interfaces (such as voids). More importantly, the NEMD simulations employ a Tersoff empirical potential that cannot reproduce the phonon dispersion of diamond correctly[147] and was developed for the GaN/SiC interface[150] rather than the GaN/diamond interface. The potential for cross-interface interaction is developed by a rough mixing rule, and the interfacial structure produced by this potential is not calibrated by the experiment to any extent. It would be worth creating a more realistic potential and investigating the interfacial reaction from the first principles.

5.2. GaN/SiC Interface. SiC is one of the three commonly used substrates for the growth of GaN (the other three are Si, GaN, and Al_2O_3). Without special notation, SiC is referred to the 4H phase of SiC, which is more commonly studied than the other phases. Since SiC has a high thermal conductivity of ~350 W m^{-1} K^{-1},[169] which is higher than most other materials although lower than diamond, it is an ideal substrate for the thermal management of GaN. The first reported TBC of the GaN/SiC interface is about 8.3 MW m^{-2} K^{-1} by Kuzmik et al. in 2007.[149] No details were given regarding the interface quality. Later in 2012, Cho et al. measured an MOCVD-grown GaN/SiC interface with a ~36 nm-thick AlN interlayer using TDTR and showed a significantly larger TBC of ~200 MW m^{-2} K^{-1}.[78,148] During the epitaxial growth, a layer of AlN transition layer is usually added because of the lattice mismatch between GaN and SiC. Several other works have reported similar TBCs with different growth methods and interlayer contents, which are summarized in Table 2, in the order of interlayer thickness. A similar trend as for GaN/diamond interface is observed, i.e., thinner interlayer results in higher TBCs. The highest TBC achieved to date is ~230 MW m^{-2} K^{-1}. The first work that achieved this record-high TBC was done by Ziade et al. with a clean interface without an interlayer using the MBE growth method in 2015.[80] Note that the direct growth of GaN on SiC would sacrifice the quality of the GaN layer. In 2019, Mu et al. achieved a similar record-high TBC by using room-temperature SAB, followed by 1000 °C annealing.[106] Different from epitaxial growth, SAB can directly integrate high-quality single-crystal GaN with high-quality single-crystal SiC. Before the annealing, the interface contains a ~3 nm amorphous SiC interlayer, which gave a lower TBC value of ~170 MW m^{-2} K^{-1}. After annealing, the amorphous layer turned to crystalline, resulting in a high TBC of ~230 MW m^{-2} K^{-1}. The SAB method followed by high-temperature annealing could be a simple and effective method to achieve high TBC interfaces. In comparison, MBE growth is slow and expensive and may not work for some materials like GaN and diamond due to lattice mismatch and thermal expansion mismatch.

The higher TBC of GaN/SiC than GaN/diamond is understandable since the phonon spectra mismatch between GaN and SiC is smaller. Compared to the GaN/diamond interface, many more simulation works have been conducted for GaN/SiC interfaces. This is because GaN and SiC share a similar cell structure, and the interatomic potential between GaN and SiC can be readily constructed by mixing the individual potentials of GaN and SiC using the mixing rule. Since the interaction between GaN and SiC was not derived from first-principles simulations and the interface structure was not validated against the experiment, it is expected that the obtained TBC values could not match experimental data, as seen in Table 2.

The first atomistic simulation work was done by Hu et al.[150] in 2011. Through NEMD simulations with the Tersoff potential, they obtained the TBC of the GaN/SiC interface with a nonepitaxial layer of about 520 MW m^{-2} K^{-1}. The overprediction compared to experimental data is because the simulations assumed perfect interfaces and oversimplified interatomic potentials. Two higher TBC values, i.e., ~800 and 570−630 MW m^{-2} K^{-1}, were achieved by incorporating a layer of 1 nm-long, 8 nm-wide interlaced teeth, and a 1 nm AlN film between GaN and SiC, respectively, indicating that the nanoengineering can significantly improve the TBC. Subsequently, Hu et al.[151] conducted similar NEMD simulations for GaN/SiC and GaN/monolayer graphene/SiC interfaces and obtained 420 and 601 MW m^{-2} K^{-1}, respectively, indicating that adding graphene as an interlayer can significantly improve the TBC. Also, they found an unexpected temperature drop at the near-interface region, which suggests that the interfacial thermal transport was not dominated by the interface thermal resistance but by the resistance at the near-interface region. However, this phenomenon has not been observed by other studies yet.

In 2016, Lee et al.[152] demonstrated via NEMD simulations that by introducing an experimental achievable nanostructured interface with square-shape pillar arrays for GaN/SiC, the TBC can be promoted by 42% from 470 to 670 MW m^{-2} K^{-1}. Whereafter in 2017, they studied the impacts of interlayer (made of artificial wurtzite compound AB) for the GaN/SiC interface,[153] i.e., GaN/AB/SiC. By varying the mass ratio between elements A and B, they were able to probe the role of optical phonons in the intermediate layer in affecting the TBC. It was found that the maximum TBC can reach 971 MW m^{-2} K^{-1}, 22% higher than that of the bare SiC/GaN interface by setting the m_A = 51.7 and m_B = 10.3 a.m.u. The results reveal that the optical phonon spectra, which are sensitive to relative atom mass, can significantly impact thermal transport. The values obtained in this study are a bit larger than widely reported (470−530 MW m^{-2} K^{-1}) in related papers by MD simulations. This is because GaN and SiC only differ from each other in atomic masses in their model—they ignored the differences in lattice structures and interatomic potentials of GaN and SiC for the sake of convenience. The lattice mismatch, atomic rearrangement, and different interatomic potentials can all introduce extra thermal resistance.

Afterward, Lee et al.[155] investigated the role of isotope via NEMD. Their calculation results demonstrated that the ^{15}N doping within a skin depth of 4 nm could increase the TBC by as much as 18% from 470 to 555 MW m^{-2} K^{-1} compared to the isotopically pure case. The augmentation in TBC by isotopes was attributed to the enhancement of preinterface phonon scattering induced by isotopes, which facilitates the redistribution of phonon energy to favor a better overall interfacial thermal transport. Similarly, the impact of light atoms on the TBC of the GaN/SiC interface was studied by Li et al. using the NEMD method in 2019.[154] It was found that substituting Ga atoms with lighter atoms (e.g., boron) with 50% concentration near the interface could increase the TBC from 495 to 755 MW m^{-2} K^{-1}, an improvement as high as 50% when the interlayer is 2.5 nm thick. Decreasing the content of light atoms or just introducing light atoms interstitially can lead to a less significant enhancement on TBC as shown in the table. Their spectral analysis indicates that light atoms with high velocities can introduce mid- and high-frequency phonon modes which can couple well with the counterparts on the

https://doi.org/10.1021/acsami.3c02507
ACS Appl. Mater. Interfaces 2023, 15, 29655−29673

other side of the interface, consequently enhancing the TBC. These simulations provide valuable guidance for TBC improvement but also present a huge gap between simulation and experiment.

5.3. GaN/Si Interface. Similar to SiC, Si is a commonly used substrate of GaN. Due to the large lattice mismatch between Si and GaN, an AlN transition film is commonly used as an interlayer to release stress. Thicker intermediate AlN leads to a higher quality of GaN but possibly reduces the TBC at the same time. Both MBE and MOCVD can well control the growth thickness of AlN. Using MBE, Cho et al.[78,148] grew GaN on Si containing a 38 nm-thick AlN interlayer in 2012. The TBC was reported as 188 MW m^{-2} K^{-1} at room temperature[78,148] and was later corrected to 128 MW m^{-2} K^{-1}.[79] In 2015, Yates et al.[100] grew a GaN/Si interface by MOCVD with a 100 nm-thick AlN interlayer and measured the TBC of 263 of MW m^{-2} K^{-1}. This larger TBC with thicker interlayer is counterintuitive and might be because of the higher GaN quality.

Much recently, Yang et al.[83] estimated the overall heat dissipation performance of GaN/Si interface with commonly used solders like AuSn as bonding layers, instead of AlN, grown by PVD. The total TBC was shown to be 16.5 MW m^{-2} K^{-1}, substantially lower than others' data. They pointed out that the reduction in TBC was attributed to the mismatch of phonon frequencies across the interface and that the introduction of a metal bonding layer is not naturally beneficial for the overall TBC. The related studies are summarized in Table 2.

5.4. GaN/AlN Interface. GaN/AlN interface has received interest because AlN is commonly and intentionally formed between GaN and substrates as an interlayer as seen in the previous sections. Knowing the TBC of the GaN/AlN interface is necessary to understand the role of the AlN interlayer between GaN and substrates. Therefore, several theoretical works have been conducted to simulate GaN/AlN interfacial thermal transport, also partially because the interatomic potential between GaN and AlN can be readily constructed using the mixing rule, as summarized in Table 2. On the experimental side, the only reported value is about 620 MW m^{-2} K^{-1} for GaN/AlN superlattice with long periods.[156]

The first simulation work was done by Liang et al. in 2014.[157,158] They developed a Stillinger−Weber (SW) potential to calculate the TBC of the GaN/AlN interface via NEMD and Green−Kubo equilibrium MD (EMD) simulations. The NEMD and EMD gave comparable TBC values in the range of 1150−1300 MW m^{-2} K^{-1}, being much larger than the experimental value. Bao et al.[161] calculated the TBC of the GaN/AlN interface using NEMD simulations with a Lennard-Jones (LJ) potential and obtained 780 W m^{-1} K^{-1}. Their Monte Carlo simulations, fully based on the first-principles, predict a TBC of about 870 MW m^{-2} K^{-1}. Another first-principle-based nonequilibrium Green's function calculation in the harmonic limit by Polanco et al.[159] in 2019 obtained a low value of 300 MW m^{-2} K^{-1}. These results demonstrate large gaps between different simulations and between simulations and experiements.

Simulations also showed that the TBC of the GaN/AlN interface can be largly tuned by interfacial engineering. Three types of GaN/AlN interfacial morphologies, namely wurtzite, rock-salt, and amorphous, were explored by Wang et al.[160] using NEMD in 2021. Their results demonstrated that the TBC can be significantly enhanced by recrystallizing the amorphous AlN to rock-salt one, from 149 to 825 MW m^{-2} K^{-1}. Sun et al.[162] further investigated the role of misfit dislocation structure via NEMD with three different interatomic potentials, i.e., SW, mixing rule-based Tersoff, and transferable Tersoff potentials. They demonstrated that similar misfit dislocation networks and core structures were produced by all three interatomic potentials. With those defects, the TBC was shown to be 496, 2440, and 1933 MW m^{-2} K^{-1}, a reduction of 47.1%, 21.9%, and 40.1%, respectively, compared to that without misfit dislocation. These results also show a strong impact of the choice of interatomic potential on the predicted TBCs.

5.5. GaN/BAs Interface. Boron arsenide (BAs) has received great interest since 2013 when it was theoretically predicted to have an ultrahigh thermal conductivity of 2200 W m^{-1} K^{-1}, comparable to diamond, by Lindsay et al. by first-principles three-phonon scattering calculations. In 2017, Feng et al. revised the prediction to ∼1400 W m^{-1} K^{-1} by including four-phonon scattering. This value was supported by various experiments in 2018. Since then, BAs has been recognized as the second-highest thermal conductivity material in nature. Naturally, it is of great interest to check whether BAs can be used as thermal management substrates for WBGSs. However, there is not much work done yet as this material is new and no large crystals can be grown for now. The only work reported on this system so far is done by Kang et al.[101] in 2021, in which a metamorphic heteroepitaxy method was applied to relax the strain with a 2 nm amorphous Al_2O_3 layer introduced as an adhesion layer, considering the crystal structures of BAs (zinc blende cubic) and GaN (wurtzite) are different. A follow-up oxygen plasma treatment was then used to activate interface bonds, and the sample was annealed at 500 °C for 24 h in a vacuum. The TBC of the GaN/BAs interface was measured by TDTR as ∼250 MW m^{-2} K^{-1} without reporting measurement and data fitting details, which is high compared to other TBCs reported in this review. The authors also suggested that the TBC of the GaN/BAs interface could be further enhanced through optimization of the resistance contribution from the oxide interlayer.

5.6. GaN/Oxides Interfaces. GaN/oxides interfaces have been extensively studied since oxides are the commonly used substrates due to their insulation nature. The related experimental and computational studies are summarized in Table 2. Sapphire (Al_2O_3) is one of the most extensively used substrates due to its low cost. The first experimental GaN/Al_2O_3 TBC was reported as 8.3 MW m^{-2} K^{-1} by Kuzmík et al. in 2007.[149] However, they stated that the output signal was not that sensitive to the TBC value, which resulted in a large uncertainty. In 2014, Wang et al.[163] obtained 10 MW m^{-2} K^{-1} by TDTR with MOCVD and by the 3ω method[164]. For GaN/SiO_2 interface,[164] the value was about 15 MW m^{-2} K^{-1}, higher than that of GaN/Al_2O_3. Though the reported TBC values for GaN/oxides are between 8−15 MW m^{-2} K^{-1}, these data may need re-examination because the oxides themselves have large thermal resistance compared with the interfaces, which leads to low sensitivity in the measurement. Different temperature dependencies of these two interfaces were observed during the measurement, i.e., the TBC of GaN/SiO_2 increases dramatically with increasing temperature, whereas that of GaN/Al_2O_3 decreases with increasing temperature. Some of the possible reasons for such difference are the migration of oxygen across the interface and phonon inelastic scattering.[164] For all these interfaces, the interfacial nanostructure is unclear, which

https://doi.org/10.1021/acsami.3c02507
ACS Appl. Mater. Interfaces 2023, 15, 29655−29673

Table 3. Thermal Boundary Conductance of Si/Diamond and Si/SiC Interfaces

	Growth/ Simulation Method	Interlayer	Measurement Method/Interatomic Potential	TBC (MW m^{-2} K^{-1})	Ref.
Si/diamond	Graphoepitaxy	None	TDTR	64	Cheng 2019 [76]
Si/diamond	CVD	None	TPS	50-100	Goyal 2010 [95]
Si/diamond	Unclear	Unclear	Unclear	30	Goodson 1994 [173]
Si/diamond	CVD	~10 nm amorph.	Joule-heating	>67	Goodson 1995 [97]
Si/diamond	CVD	Unclear	Laser pulse	18	Klokov 2010 [98]
Si/diamond	CVD	Unclear	3ω method	50	Mohr 2017 [99]
Si/diamond	Graphoepitaxy	47×69 nm teeth	TDTR	105	Cheng 2019 [76]
Si/diamond	Graphoepitaxy	105×210 nm teeth	TDTR	80	Cheng 2019 [76]
Si/diamond	Simulations	None	NEMD Tersoff (45nm)	381	Cheng 2019 [76]
Si/diamond	Simulations	2 nm a-C	NEMD Tersoff (45nm)	378	Cheng 2019 [76]
Si/diamond	Simulations	None	NEMD Brenner (6nm)	238	Khosravian 2013 [174]
Si/diamond	Simulations	None	NEMD Brenner (13nm)	482	Khosravian 2013 [174]
Si/SiC	Low-temp. CVD	None	TDTR	600	Cheng 2022 [175]
Si/SiC	Hydrophobic bonding	0.2–2.5nm a-SiO_2	TTR	100–250	Field 2022 [103]
Si/SiC	Hydrophilic bonding	2.5 nm a-SiO_2	TTR	80–110	Field 2022 [103]
Si/SiC	NEMD	None	Tersoff	890	Xu 2022 [77]
Si/SiC	NEMD	Interlaced teeth	Tersoff	300–1000	Xu 2022 [77]

highlights the importance of detailed materials characterizations in future studies.

ZnO was recently studied as a substrate due to its good lattice match with GaN. In 2018, Gaskins et al.[165] grew ZnO thin films heteroepitaxially on a Ga-polar GaN wafer by pulsed-laser deposition, and a 10- to 12 nm defective region with dislocations was identified. With TDTR, their measured TBC is 490 MW m^{-2} K^{-1}, which is much higher than that of Al_2O_3 or SiO_2 interfaces, showing a bright prospect. They also conducted DMM and AGF simulations and obtained 295 and 240 MW m^{-2} K^{-1}, respectively, smaller than the measured data. Two potential explanations were given. On the one hand, the TBC may be intrinsic to the phonon modes in the ZnO and not necessarily related to a “transmission” of modes restricted by the vibrational states on the other side of the interface. On the other hand, the presence of anharmonic interactions at the interface, which is ignored in DMM and AGF, may contribute to the TBC. The current study on GaN and oxides interfaces are limited, and further work is needed to substantially improve the TBC.

5.7. GaN/Metal Interfaces. GaN/metal interfaces are also important since metals are required in electronics to form Ohmic and Schottky contacts. Also, metals are commonly used in the TDTR measurement as a transducer. The TBC values are summarized in Table 2. Compared to GaN/nonmetal interfaces, the thermal transport through GaN/metal interfaces is more complicated since it may involve thermal transport from the phonons of GaN to the electrons of metals.

In Table 2, we summarized the TBCs between GaN and Al, Au, and Cr. The highest values achieved experimentally for them are 400, 250, and 230 MW m^{-2} K^{-1}, respectively. The first available TBC of GaN/metals interfaces was reported by Stevens et al.[114] in 2005. They measured the TBC of GaN/Al and GaN/Cr interfaces to be 190 and 230 MW m^{-2} K^{-1}, respectively. In 2014, Donovan et al.[12] measured the TBCs of GaN/Al, GaN/Au, and GaN/Ti/Au interfaces as 92, 55, and 250 MW m^{-2} K^{-1}, respectively, which suggested that the GaN/Ti/Au interface provided a better thermal management solution in GaN devices compared to Al and pure Au because Ti can enhance adhesion between GaN and Au. A clear dependence of TBC on metallic contact and the operating temperature was found and explained. In the same year, Wang et al.[163] and Cho et al.[79] separately estimated the TBC of the GaN/Al interface as 160 and 47−161 MW m^{-2} K^{-1}, respectively, during the measurement of the GaN/dielectric interface by TDTR with Al as a transducer covering the GaN thin film. Likewise, Freedman et al.[166] measured the TBC of GaN/Au and GaN/Cr interfaces as 180 MW m^{-2} K^{-1} during the estimation of phonon MFP-dependent thermal conductivity for GaN with Au and Cr as the transducer by FDTR in 2013. In 2021, the TBC of the GaN/Al interface was also investigated by Koh et al.[81] using TDTR. As the Al film was *in situ* deposited on the GaN film under an ultrahigh vacuum, there were few defects at the interface. Thus, they reported to date the highest value of TBC, which was about 400 MW m^{-2} K^{-1}. This result is also in good alignment with their calculation results by the nonequilibrium (NE) Landauer approach, considering the elastic phonon scattering process, which suggested that inelastic electron or phonon processes contributed little to the TBC of GaN/Al.

On the simulation side, the results of the GaN/Al interfaces are summarized in Table 2. In 2013, with the LJ potential, Jones et al.[167] obtained 211 MW m^{-2} K^{-1} by NEMD simulations. As for the electron’s role in TBC, they suggested that electron-mediated transport had little effect on thermal resistance by coupling the MD to a two-temperature model (i.e., electrons and phonons have difference temperatures). Zhou et al.,[168] otherwise, adopted the SW potential in NEMD simulations and found that the TBC the GaN/Al interface with the Al−Ga contact was 99 MW m^{-2} K^{-1}, which was increased to 102 MW m^{-2} K^{-1} if 3 nm long, 7 nm-wide interlaced teeth were introduced at the interface. They also found that the Al-N contact Al also resulted in higher TBC, i.e., 172 MW m^{-2} K^{-1}. These values are smaller than experimental data, which could be because of the inaccuracy of the interatomic potential. Zhou et al. highlighted that their objective was not to extract quantitative data for specific materials, but rather to discover the functional dependence of TBC on the type and quality of the interfacial structures. Hence, the size of their simulation domain was not large, and the effect of electrons was neglected.

5.8. Si/Diamond Interface. Si/diamond interface is also important due to the high potential of using diamond as the

https://doi.org/10.1021/acsami.3c02507
ACS Appl. Mater. Interfaces 2023, 15, 29655−29673

Table 4. Thermal Boundary Conductance between β-Ga_2O_3 and Other Materials

β-Ga_2O_3/substrate	Growth/Simulation Method	Interlayer	Method	TBC (MW m^{-2} K^{-1})	Ref.
Ga_2O_3/diamond	Transferred	None (van der Waals)	TDTR	17	Cheng 2019 [66]
Ga_2O_3/diamond	ALD	None (ultra-clean)	TDTR	179	Cheng 2019 [66]
Ga_2O_3/diamond	ALD	Ga-rich	TDTR	136	Cheng 2019 [66]
Ga_2O_3/diamond	ALD	O-rich	TDTR	139	Cheng 2019 [66]
Ga_2O_3/diamond	Hydrophilic bonding + 250 °C annealing	None (ultra-clean)	-	-	Matsumae 2020 [104]
Ga_2O_3/SiC	SAB + 800 °C ann.	Unclear	TDTR	150	Cheng 2021 [176]
Ga_2O_3/SiC	SAB	30nm Al_2O_3 + 3.5nm a-SiC	TDTR	72	Cheng 2020 [61]
Ga_2O_3/SiC	SAB + 800 °C ann.	30nm Al_2O_3 + 2nm a-SiC	TDTR	65	Cheng 2020 [61]
Ga_2O_3/SiC	SAB	9.4nm Al_2O_3 + 2.7nm a-SiC	TDTR	100	Cheng 2020 [61]
Ga_2O_3/SiC	SAB + 800 °C ann.	9nm Al_2O_3 + 2nm a-SiC	TDTR	88	Cheng 2020 [61]
Ga_2O_3/SiC	SAB	1.8nm a-Ga_2O_3 + 2.2nm a-SiC	-	-	Xu 2019 [108]
Ga_2O_3/SiC	SAB + 1000 °C ann.	1.5nm crystal defective layer	TDTR	244	Liang 2022 [177]
Ga_2O_3/SiC	SAB + 200 °C ann.	1.3nm a-Ga_2O_3 + 2.2nm a-SiC	-	-	Xu 2019 [108]
Ga_2O_3/diamond	Theory	None	DMM	312	Cheng 2019 [66]
Ga_2O_3/Au	Wedge deposition	None	FDTR	45	Aller 2019 [178]
Ga_2O_3/Au	E-beam evaporation	Defective layer	TDTR	31.2	Shi 2021 [63]
Ga_2O_3/Ti	E-beam evaporation	Defective layer	TDTR	17.4	Shi 2021 [63]
Ga_2O_3/Ni	E-beam evaporation	Defective layer	TDTR	82.7	Shi 2021 [63]
Ga_2O_3/Al	E-beam evaporation	Defective layer	TDTR	81.7	Shi 2021 [63]
Ga_2O_3/Au	Wedge deposition	2.5 nm Cr	FDTR	530	Aller 2019 [178]
Ga_2O_3/Au	Wedge deposition	5 nm Ti	FDTR	260	Aller 2019 [178]
Ga_2O_3/Au	Wedge deposition	>3 nm Ni	FDTR	410	Aller 2019 [178]
Ga_2O_3/Au	Theory	None	DMM	71.2	Shi 2021 [63]
Ga_2O_3/Ti	Theory	None	DMM	103	Shi 2021 [63]
Ga_2O_3/Ni	Theory	None	DMM	126	Shi 2021 [63]
Ga_2O_3/Al	Theory	None	DMM	139.6	Shi 2021 [63]
Ga_2O_3/Cr	Theory	None	DMM	148.7	Shi 2021 [63]

substrate for the thermal management of Si devices.[170,171] However, the TBC values obtained as of now are not high due to the low quality of interfaces, as summarized in Table 3. During the growth of Si/diamond heterostructures, diamond seeds that are randomly dispersed on Si gradually grow and merge as a film. As a result, the diamond near the interface is nanocrystalline with small grain sizes. Sometimes the thermal conductivity of synthetic diamonds near the Si/diamond interface is even lower than Si at room temperature.[94] The first reported value is 30 MW m^{-2} K^{-1} by Goodson et al.,[172] but no details about the growth or measurement method are given. Later, they reported a > 67 MW m^{-2} K^{-1} value for a CVD-grown Si/diamond interface with a 10 nm amorphous interlayer.[96] Goyal et al.[94] found the TBC varies between 50−100 MW m^{-2} K^{-1} with various synthetic diamond grain sizes and film thicknesses by transient plane source (TPS). Klokov et al.[97] reported 18 MW m^{-2} K^{-1} by the laser pulse method for the polycrystalline diamond film deposited on a silicon substrate. In comparison, Mohr et al.[98] extracted the TBC between Si and nanocrystalline diamond (NCD) films to be 50 MW m^{-2} K^{-1} using the 3ω method. For these samples, the interface condition was not reported.

Cheng et al.[76] improved the TBC of Si/diamond interfaces significantly by graphoepitaxy in 2019. The 105 nm-long, 210 nm-wide interlaced teeth at the interface increase the TBC of the flat Si/diamond interface from 64 MW m^{-2} K^{-1} to 80 MW m^{-2} K^{-1}, which is further increased to 105 MW m^{-2} K^{-1} by 47 nm-long, 69 nm-wide interlaced teeth, an indication of a strong correlation between the shape and size of the interlaced teeth and TBC. This is the highest Si/diamond TBC value reported to date. They attributed the immense increase of TBC to the enlarged contact area between Si and diamond. Since the STEM image in this study reported a presence of an amorphous layer between the crystalline Si and diamond surfaces, the influence of the crystal phase on TBC was investigated by NEMD simulations with a Tersoff potential. The simulated results show that the amorphous layer should play a negligible role in the TBC. However, the simulation result (∼380 MW m^{-2} K^{-1}) is much higher than the measured value of 64 MW m^{-2} K^{-1} for the flat interface. The observed discrepancy in the TBC values between the experimental and simulation results was mainly attributed to the inaccuracy of the available interatomic potentials and the size effect of the simulation domains. Similar simulation research was carried out by Khosravian et al.[173] in 2013 with the Brenner potential and reported TBCs of 238−482 MW m^{-2} K^{-1} with small system sizes. Since these MD simulation results are consistently higher than the available experimental data, extensive simulation work that includes underlying experimental interface type and quality might be needed to quantitively validate experimental findings.

5.9. Si/SiC Interface. Si/SiC interface serves as a competitive alternative to silicon/oxides interfaces because of the improved thermal management in power conversion and harsh environment applications. However, only a handful of studies on TBC measurement are available to date as illustrated in Table 3. Field et al. directly bonded wafer Si/SiC by hydrophilic and hydrophobic methods.[102] The hydrophilic bonding results in a uniform 2.5 nm-thick amorphous interlayer with a TBC of 80−110 MW m^{-2} K^{-1}. In contrast, the hydrophobic bonding results in an interlayer with varying thicknesses of 0.2−2.5 nm and an improved TBC of 100−250 MW m^{-2} K^{-1}.[63] Meanwhile, Cheng et al.[174] grew 3C-SiC crystals on Si substrates by low-temperature CVD. They reported a record high TBC among semiconductor interfaces, which is above 600 MW m^{-2} K^{-1}. This is achieved mainly by growing high-quality interfaces at a low-temperature condition, which reduces the strain in 3C-SiC caused by the

https://doi.org/10.1021/acsami.3c02507
ACS Appl. Mater. Interfaces 2023, 15, 29655−29673

mismatch of thermal expansion coefficient and then prevents the formation of cracks at the interface. Regarding the simulation efforts in this system, Xu et al.[77] recently carried out the first NEMD simulations with Tersoff potential and obtained a TBC of 887 MW m^{-2} K^{-1}. They demonstrated that the TBC can be modulated broadly from 300 to 1000 MW m^{-2} K^{-1} by confining nanopatterns with a thickness on the order of nanometers, e.g., smaller than 30 nm. More work is needed to bridge the TBC values gap between simulations and experiments.

5.10. β-Ga_2O_3/SiC and β-Ga_2O_3/Diamond Interfaces. The study of β-Ga_2O_3 interfaces is still at an early stage. The first TBC was reported in 2019 by Cheng et al.,[66] in which a (100) oriented β-Ga_2O_3 nanomembrane was transferred on a single crystal (100) CVD diamond substrate and measured a TBC of 17 MW m^{-2} K^{-1} by TDTR. They attributed the low TBC to the van der Waals bonding, which results in low phonon transmission due to the weak adhesion. They further deposited β-Ga_2O_3 onto ultraclean single crystal diamond substrates by ALD and realized a covalently bonded interface,[60] which resulted in a significantly higher TBC of 179 MW m^{-2} K^{-1}. With different *in situ* pretreatments of the diamond surfaces, they also found that the TBC of the Ga-rich and O-rich β-Ga_2O_3/diamond interfaces is about 20% smaller than that of the clean interface, indicating the significant impact of interface chemistry on TBC. In 2020, Matsumae et al.[103] directly bonded β-Ga_2O_3 with diamond by room-temperature SAB followed by annealing at 250 °C in the ambient air. TEM images of the β-Ga_2O_3/diamond bonding interface revealed an atomically bonded, high-quality surface, without any nano-voids, cracks, or intermediate layer. This study extensively focused on the interface chemistry and structural properties, and the TBC of the interface was not measured.

As for β-Ga_2O_3/SiC interfaces, Cheng et al.[61] reported a scalable wafer-scale strategy to integrate nanoscale monocrystalline β-Ga_2O_3 thin films on SiC substrates heterogeneously via ion-cutting and room-temperature SAB. Four samples with different Al_2O_3 interlayer thicknesses and different annealing conditions (corresponding to different a-SiC thicknesses) were produced and measured by TDTR as summarized in Table 4. The TBC was shown to be varying from 65 to 100 MW m^{-2} K^{-1}. The TBC value increases with decreasing Al_2O_3 interlayer thickness but reduced slightly after the thermal annealing.[115] Using SAB with Si-containing Ar ion beams, Xu et al.[107] were able to achieve a β-Ga_2O_3/SiC interface with only a 1.8 nm Ga_2O_3 + 2.2 nm amorphous SiC interlayer. By an annealing process at 200 °C, the amorphous Ga_2O_3 layer shrunk to ∼1.3 nm. However, they did not measure the TBC. Later, Cheng et al.[175] implemented the same SAB procedure, but with a different annealing temperature (800 °C), resulting in a high-quality β-Ga_2O_3/SiC interface for which the measured TBC reached 150 MW m^{-2} K^{-1}. More recently, Liang et al.[176] reported a record high TBC value of 244 MW m^{-2} K^{-1} for β-Ga_2O_3/SiC interfaces owing to a superior-quality heterointerface. The interfacial region is composed of a crystalline defective layer of 4.5 nm after the RT SAB, which is reduced further to 1.5 nm after 1000 °C annealing.

The only available simulation work on the TBC of β-Ga_2O_3/SiC and β-Ga_2O_3/diamond interfaces was reported by Cheng et al.[66] in 2019. With the DMM model, they calculated the TBC of β-Ga_2O_3/diamond to be 312 MW m^{-2} K^{-1}, which was much higher than their experimental results. They attributed the difference to the interfacial bonding and real contact area at the interface.

5.11. β-Ga_2O_3/Metal Interfaces. The TBCs of β-Ga_2O_3/metals interfaces reported in the literature are summarized in Table 4. Aller et al.[177] deposited Au on top of bare as well as Cr, Ti, and Ni-covered β-Ga_2O_3 using the wedge deposition method. The TBCs of Au/β-Ga_2O_3, Au/Cr/β-Ga_2O_3, Au/Ti/β-Ga_2O_3, and Au/Ni/ β-Ga_2O_3 interfaces were measured by FDTR. They found the inverse-U-shaped correlation between the TBC and layer thickness where TBC first increases with increasing interlayer metal thickness before reaching saturation and then decreases. Among these samples, the interface with 2.5 nm Cr as interlayer has the highest TBC value, which reaches 530 MW m^{-2} K^{-1}. All three samples with metal interlayers showed much higher TBC than the bare Au/β-Ga_2O_3 interface. They pointed out that the oxide layers were formed during the deposition process, without which the TBC could be even higher. Shi et al.[63] conducted both theoretical and experimental studies for a range of different β-Ga_2O_3/metals interfaces, i.e., β-Ga_2O_3/Au, β-Ga_2O_3/Ti, β-Ga_2O_3/Ni, β-Ga_2O_3/Al, and β-Ga_2O_3/Cr. They found that the TBC values of those interfaces at room temperature vary from 90 to 150 MW m^{-2} K^{-1}. For the ohmic contact metals, β-Ga_2O_3/Cr interfaces demonstrate the highest TBC of 149 MW m^{-2} K^{-1}, while for Schottky contact metals, β-Ga_2O_3/Ni interfaces show the highest TBC of 126 MW m^{-2} K^{-1}. They also concluded that the experimentally measured TBC values from TDTR are typically lower than the DMM results. According to their analysis, the metal cutoff frequency should play the main role in the TBC followed by other factors, like chemical reactions and defects. Since there are only two relevant studies published, further studies are desired.

6. DISCUSSION ON INTRINSIC TBCS

Based on Section 5, we have summarized the state-of-the-art TBC values of various interfaces achieved experimentally in Figure 7. Regardless of the different interfacial structures, the highest TBC values achieved for various structures can be

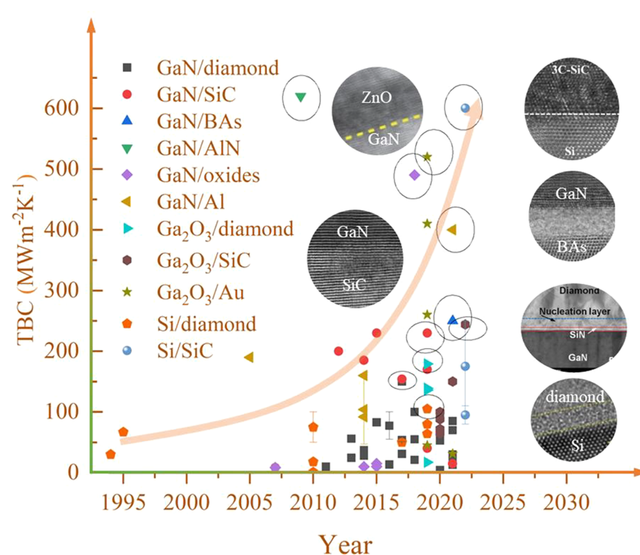

Figure 7. Experimental TBC improvement of (U)WBGS heterostructures in the past two decades. The state-of-the-art TBC achieved for each heterostructure is circled. The available atomic resolution images for the state-of-the-art works are shown.

https://doi.org/10.1021/acsami.3c02507
ACS Appl. Mater. Interfaces 2023, 15, 29655−29673

ordered from high to low as follows: GaN/AlN > Si/SiC > Ga_2O_3/Au ≈ GaN/ZnO > GaN/Al > GaN/SiC ≈ GaN/BAs ≈ Ga_2O_3/SiC > Ga_2O_3/diamond > GaN/diamond > Si/diamond. The order can be understood by comparing the phonon spectra mismatches between WBGSs and UWBGSs as well as the substrates and contacts, as shown in Figure 8. We distinguish the acoustic from optical phonon frequency ranges using different colors. Since acoustic phonons dominate the elastic transmission as well as thermal conductivity of bulk materials, they are considered the dominant heat carriers for interfacial thermal transport, despite that optical phonons are found to carry considerable heat across interfaces via inelastic transmission in MD simulations. As seen in Figure 8, diamond has the widest acoustic phonon spectra, being more than two times those of all the other materials, leading to a high phonon mismatch. This explains why diamond-related interfaces exhibit the lowest TBCs. GaN has a good match with AlN and ZnO and thus has high TBCs. Si and SiC have a good acoustic frequency match and thus have a high TBC. Interestingly, some are counterintuitive such as Ga_2O_3/Au interface, which does not have a good phonon match but shows a high TBC. This could be a measurement error/uncertainty or complex inelastic effect. From Figure 8, it can also be guessed that certain materials might be appropriate intermediate layers to bridge the acoustic spectra of other interfaces. For example, SiC can bridge Si/diamond; AlN and Si_3N_4 can bridge GaN/diamond; Al_2O_3 can bridge Ga_2O_3/SiC; SiC, Si, AlN, Si_3N_4 can bridge Ga_2O_3/diamond; no bridge is needed for Al_2O_3 and Al. In a word, Figure 8 could serve as guidance for future research efforts.

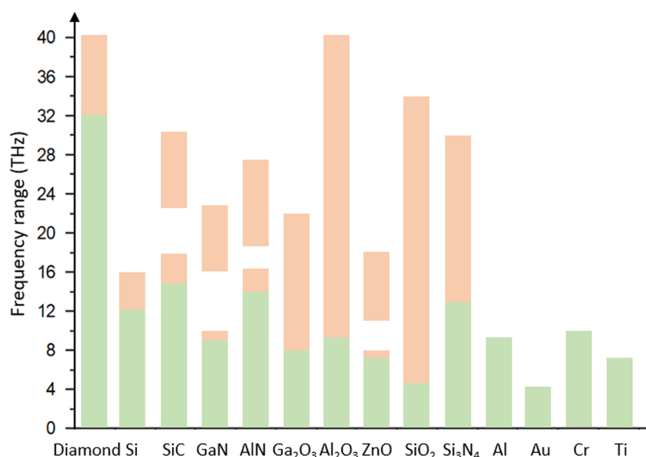

Figure 8. Phonon frequency ranges of various materials. Green and orange bars represent acoustic and optical phonons, respectively.

7. CONCLUSIONS AND OUTLOOK

The past decades have witnessed the rapid improvement of thermal boundary conductance across WBGS and UWBGS heterostructures, and in the coming decade, more mature experimental and reliable simulation works will be emerging to further push the TBC values. A foremost and natural question to answer is: What are the theoretical upper limits of the TBCs for these interfaces if they exist? This is an ambitious question since there are numerous interlayer materials and geometries that can be introduced between two materials to facilitate heat transfer. To answer this question, an accurate theoretical or simulation method is required. DMM and AMM can give theoretical elastic limits, but they do not consider inelastic phonon transmission and cannot be viewed as the theoretical upper limit. Future research that constructs machine learning interatomic potential with a DFT accuracy for interfaces will be valuable, and it will open an avenue for accurate TBC predictions and interfacial structure optimization. Machine learning molecular dynamics (MLMD) is expected to be the focus area in the next decade since it has both the advantage of classical MD (high efficiency) and *ab initio* MD (high accuracy).[74] A follow-up question is: How to realize the theoretical upper limits? Current experiments have only tried a finite number of interlayer materials, thicknesses, and geometries. However, a comprehensive understanding of the theoretical limit requires a large number of experimental studies aided by supporting theoretical simulations. Since none of the experiments in the literature has realized an atomically flat and clean interface for the heterostructures reviewed in this article, a natural question is: What are the TBCs for atomically flat and clean heterostructures? Although they can construct atomically flat and clean interfaces, current simulation methods cannot predict credible results, as discussed in Section 4. Therefore, the experimental effort that can grow an atomically flat and clean interface will be of great scientific significance. Simulation methods that can accurately predict TBCs are urgently needed. More direct comparisons between experiments and simulations for the heterostructures reviewed in this article are needed. It is worth answering whether an interlayer changes the temperature-dependent properties (notably at higher temperatures), which can help understand how the inelastic scattering can be promoted within an interlayer at increased temperature. We expect with the advancement of the experimental bonding method and the accurate atomistic simulations, the TBCs of WBGS and UWBGS heterostructures will experience another leap in the coming decades. Based on different systems, we listed possible future research directions as follows.

7.1. GaN/Diamond. (1) Since TBC increases with decreasing interlayer thickness generally, a natural question is whether the TBC can be further improved if the thickness of the interlayer can be reduced below 5 nm; for example, 1 nm. In addition, will no interlayer give the upper limit of TBC? On the one hand, the works that reported noninterlayer only showed TBC values of about 4.5−21 MW m^{-2} K^{-1},[52,84,85] as shown in Table 2. As pointed out by the authors, this might be because there are voids at the interface for the CVD-grown nanocrystalline diamond on GaN without interfacial protective layers. On the other hand, it is a big challenge to form direct bonding between GaN and diamond interfaces due to the large lattice and thermal expansion mismatch. So far, only Liang et al. reported one method to achieve that experimentally, but they do not measure any thermal properties, such as TBC of the samples. Normally, an interlayer is necessary for protecting GaN in order to create a relatively good interface. Nonetheless, the role of the 5 nm interlayer might also provide a phonon vibrational density of state bridge between GaN and diamond. Future studies providing the direct integration methods between these two materials and revealing the mechanisms of TBC enhancement by interlayers with certain thicknesses are of interest. (2) It is found that the same thickness of AlN gives lower TBC than what SiN_x gives, despite the higher thermal conductivity of AlN. What are the reasons behind that? A theoretical simulation or model is needed to provide a theoretical explanation of the observed experimental finds

https://doi.org/10.1021/acsami.3c02507
ACS Appl. Mater. Interfaces 2023, 15, 29655−29673

while guiding future experimental efforts for interlayer material selection. (3) The room-temperature SAB bonded GaN/diamond shows a TBC of 92 MW m^{-2} K^{-1}, which contains amorphous layers of diamond and silicon. An annealing process that can convert amorphous interlayer to crystalline is expected to be a promising approach to improve the TBC further. (4) Since interlaced teeth structures are effective in improving TBCs, can we construct interlaced teeth between GaN and diamond? To have the benefit of strengthened chemical bonding, can we introduce interlaced teeth on the interlayer material, i.e., introducing interlaced teeth between GaN and SiN_x as well as between SiN_x and diamond? (5) Current simulations for GaN/diamond interface are still based on empirical interatomic potential mixed from bulk materials potentials. MLMD that can describe the interfacial properties is urgently needed.

7.2. GaN/SiC. All MD simulations demonstrated that the TBC of GaN/SiC interfaces can be promoted via nanoscale interfacial treatment. However, two potential gaps between simulations and experiments should be noted. First, the SiC studied in simulations is generally 6H-SiC instead of 4H-SiC, which is different from the experimental study. Second, the simulation results of TBC are significantly larger than the experimental data. This is probably because the interatomic potentials used in the simulations are not accurate and are not calibrated by experiments or first-principles density functional theory (DFT) calculations. Another reason might be that various defects at interfaces due to the lattice mismatch in real samples can result in TBC reduction, which is not taken into account in the simulation works. A more accurate simulation method remains to be developed to model the TBC for interfaces more realistically, which can be inspired by a much recent review.[178] A question to answer from both experiments and simulations is: Is it possible to exceed the state-of-the-art value, 230 MW m^{-2} K^{-1}, if small (∼nm) interlaced teeth or roughness are introduced?

7.3. GaN/Si. To date, no simulation was found for GaN/Si, and high-fidelity MLMD simulations are urgently needed. On the experimental side, only one interlayer material (i.e., AlN) has been tried with a large thickness (∼40 nm). Other interlayer material options (e.g., SiN_x) and thinner thicknesses (1−5 nm) are yet to be explored.

7.4. GaN/AlN. NEMD is widely adopted to simulate the TBC of the GaN/AlN interface using various interatomic potentials. However, different interatomic potentials led to quite different TBC values, and there is only one experimental report available for validation.[156] More accurate first-principles-based simulations and experimental measurements, with or without the presence of interlayers, are needed. Since GaN and AlN have a similar structure, we expect many more interfacial structural designs can be realized, compared to GaN/diamond interfaces.

7.5. GaN/BAs. As a new material, BAs has not been widely studied as a substrate. To date, only one experimental work has been reported,[101] which bonded GaN and BAs by using plasma bonding, forming an amorphous Al_2O_3 interlayer. Future directions include answering the following questions: What is the TBC of bare and clean GaN/BAs interface? What if the amorphous Al_2O_3 is annealed to be crystalline? Will the SAB method give higher TBCs? Will higher thermal conductivity interlayer materials (e.g., AlN, SiC, BN) give higher TBCs?

7.6. GaN/Metals. Limited consideration was given to the roles of electrons on TBC of GaN/metals interfaces. Although the AGF and Landauer's approach that only ignores electron−phonon interaction has successfully predicted the TBC of the clean and sharp Al/Al_2O_3 interface grown by Cheng et al.,[179] the conclusion regarding the minimal or negligible role of electron−phonon interaction in modulating TBC across the GaN/metals interface warrants more in-depth and realistic simulations and high-quality experiments studies. Moreover, the match between the experimental results and theoretically predicated data seen in Al/Al_2O_3 may not be seen in GaN/metal interfaces, and AGF calculations for these interfaces are needed to indirectly examine whether electron−phonon coupling is important. Work by Fisher's group[180] on metal/metal-silicide materials that use both experimental and computational methods indicates that (for some interfaces) the electron−phonon contribution may be up to 50%. Since GaN and metals have a vibrational mismatch, the inelastic transmission may need to be included in AGF. The recently developed AGF method that incorporates inelastic phonon transmission could be an excellent candidate.[129] Alternatively, MLMD could be a more effective method to calculate the phonon TBCs (without phonon−electron coupling across the interface).

7.7. Ga_2O_3 Interfaces. The study of Ga_2O_3 related interfaces is still in its infancy stage. There are many experimental and theoretical efforts needed. As shown in Table 4, several ultraclean interfaces with very thin interlayers have been grown, but only two published experimental data on interfaces and surfaces are available now. These interfaces are expected to have very large TBCs and are expected to be revealed in the near future. Many substrate materials and bonding parameters can be tried and tuned to increase the TBCs. In the theoretical aspect, except for the two papers mentioned in Section 5.8, there is no further MD simulation reported yet, and tremendous efforts are needed to develop interatomic potentials and guide experimental designs.

AUTHOR INFORMATION

Corresponding Author

Tianli Feng − *Department of Mechanical Engineering, University of Utah, Salt Lake City, Utah 84112, United States;* orcid.org/0000-0002-7284-5657;
Email: tianli.feng@utah.edu

Authors

Hao Zhou − *Department of Mechanical Engineering, University of Utah, Salt Lake City, Utah 84112, United States;* orcid.org/0000-0001-6499-1921
Zhe Cheng − *School of Integrated Circuits and Frontiers Science Center for Nano-optoelectronics, Peking University, Beijing 100871, China*
Leighann Sarah Larkin − *Army Research Directorate (ARD), DEVCOM Army Research Laboratory, Adelphi, Maryland 20708, United States*
Mahesh R. Neupane − *Army Research Directorate (ARD), DEVCOM Army Research Laboratory, Adelphi, Maryland 20708, United States*

Complete contact information is available at:
https://pubs.acs.org/10.1021/acsami.3c02507

Author Contributions

T.F. led the review and wrote the initial draft. H.Z. provided the major inputs for Section 5. Z.C. provided the major inputs for Section 2. Z.C., L.S.L., and M.R.N. thoroughly reviewed

https://doi.org/10.1021/acsami.3c02507
ACS Appl. Mater. Interfaces 2023, 15, 29655−29673

and revised the manuscript and provided major revisions to Section 5. All authors participated in the discussions of the writing and have approved the final version of the manuscript.

Notes

The authors declare no competing financial interest.

■ ACKNOWLEDGMENTS

T.F. and H.Z. acknowledge the support from the University of Utah startup funding, the ORAU Ralph E. Powe Junior Faculty Enhancement Award, and the INL Laboratory Directed Research and Development (LDRD) Program under DOE Idaho Operations Office under contract DE-AC07-05ID14517, Project number 23A1070-064FP. Z.C. acknowledges the Fundamental Research Funds for the Central Universities, Peking University.

■ REFERENCES

(1) Margaret, M.; Vicky, P. Semiconductor Supply Chain Deep Dive Assessment. *U.S. Department of Energy Response to Executive Order 14017; America's Supply Chains*, 2022.

(2) Wong, M. H.; Morikawa, Y.; Sasaki, K.; Kuramata, A.; Yamakoshi, S.; Higashiwaki, M. Characterization of Channel Temperature in Ga 2 O 3 Metal-Oxide-Semiconductor Field-Effect Transistors by Electrical Measurements and Thermal Modeling. *Appl. Phys. Lett.* **2016**, *109* (19), 193503.

(3) Gaska, R.; Osinsky, A.; Yang, J. W.; Shur, M. S. Self-Heating in High-Power AlGaN-GaN HFET's. *IEEE Electron Device Lett.* **1998**, *19* (3), 89−91, DOI: 10.1109/55.661174.

(4) Zhou, Y.; Ramaneti, R.; Anaya, J.; Korneychuk, S.; Derluyn, J.; Sun, H.; Pomeroy, J.; Verbeeck, J.; Haenen, K.; Kuball, M. Thermal Characterization of Polycrystalline Diamond Thin Film Heat Spreaders Grown on GaN HEMTs. *Appl. Phys. Lett.* **2017**, *111* (4), No. 041901.

(5) Irmscher, K.; Galazka, Z.; Pietsch, M.; Uecker, R.; Fornari, R. Electrical Properties of β -Ga 2 O 3 Single Crystals Grown by the Czochralski Method. *J. Appl. Phys.* **2011**, *110* (6), No. 063720.

(6) Parisini, A.; Fornari, R. Analysis of the Scattering Mechanisms Controlling Electron Mobility in β -Ga 2 O 3 Crystals. *Semicond. Sci. Technol.* **2016**, *31* (3), No. 035023.

(7) Killat, N.; Montes, M.; Pomeroy, J. W.; Paskova, T.; Evans, K. R.; Leach, J.; Li, X. N.; Özgur, Ü.; Morkoç, H.; Chabak, K. D.; Crespo, A. K.; Gillespie, J. K.; Fitch, R.; Kossler, M.; Walker, D. E.; Trejo, M.; Via, G. D.; Blevins, J. D.; Kuball, M. Thermal Properties of AlGaN/GaN HFETs on Bulk GaN Substrates. *IEEE Electron Device Lett.* **2012**, *33* (3), 366−368.

(8) Tang, D. S.; Cao, B. Y. Phonon Thermal Transport and Its Tunability in GaN for Near-Junction Thermal Management of Electronics: A Review. *Int. J. Heat Mass Transf* **2023**, *200*, No. 123497.

(9) Cheng, Z.; Shi, J.; Yuan, C.; Kim, S.; Graham, S. Thermal Science and Engineering of β-Ga2O3Materials and Devices. *Semiconductors and Semimetals* **2021**, *107*, 77−99, DOI: 10.1016/bs.semsem.2021.06.001.

(10) Montgomery, R. H.; Zhang, Y.; Yuan, C.; Kim, S.; Shi, J.; Itoh, T.; Mauze, A.; Kumar, S.; Speck, J.; Graham, S. Thermal Management Strategies for Gallium Oxide Vertical Trench-Fin MOSFETs. *J. Appl. Phys.* **2021**, *129* (8), No. 085301.

(11) Warzoha, R. J.; Wilson, A. A.; Donovan, B. F.; Donmezer, N.; Giri, A.; Hopkins, P. E.; Choi, S.; Pahinkar, D.; Shi, J.; Graham, S.; Tian, Z.; Ruppalt, L. Applications and Impacts of Nanoscale Thermal Transport in Electronics Packaging. *Journal of Electronic Packaging, Transactions of the ASME* **2021**, *143* (2), No. 020804.

(12) Donovan, B. F.; Szwejkowski, C. J.; Duda, J. C.; Cheaito, R.; Gaskins, J. T.; Peter Yang, C. Y.; Constantin, C.; Jones, R. E.; Hopkins, P. E. Thermal Boundary Conductance across Metal-Gallium Nitride Interfaces from 80 to 450K. *Appl. Phys. Lett.* **2014**, *105* (20), 203502.

(13) Sarua, A.; Ji, H.; Hilton, K. P.; Wallis, D. J.; Uren, M. J.; Martin, T.; Kuball, M. Thermal Boundary Resistance between GaN and Substrate in AlGaN/GaN Electronic Devices. *IEEE Trans. Electron Devices* **2007**, *54* (12), 3152−3158.

(14) Manoi, A.; Pomeroy, J. W.; Killat, N.; Kuball, M. Benchmarking of Thermal Boundary Resistance in AlGaN/GaN HEMTs on SiC Substrates: Implications of the Nucleation Layer Microstructure. *IEEE Electron Device Lett.* **2010**, *31* (12), 1395−1397.

(15) Waldrop, M. M. The Chips Are down for Moore's Law. *Nature* **2016**, *530* (7589), 144−147.

(16) Ball, P. Feeling the Heat. *Nature* **2012**, *492*, 174.

(17) Semiconductor Industry Association. *International Technology Roadmap for Semiconductors 2.0, 2015 Edition Executive Report*, 2016; pp 1−37.

(18) Amano, H.; Baines, Y.; Beam, E.; Borga, M.; Bouchet, T.; et al. The 2018 GaN Power Electronics Roadmap. *J. Phys. D: Appl. Phys.* **2018**, *51*, 163001.

(19) Stepanov, S. I.; Nikolaev, V. I.; Bougrov, V. E.; Romanov, A. E. Gallium Oxide: Properties and Applications - A Review. *Reviews on Advanced Materials Science* **2016**, *44* (1), 63−86.

(20) Kim, M.; Seo, J. H.; Singisetti, U.; Ma, Z. Recent Advances in Free-Standing Single Crystalline Wide Band-Gap Semiconductors and Their Applications: GaN, SiC, ZnO, β-Ga2O3, and Diamond. *J. Mater. Chem. C Mater.* **2017**, *5* (33), 8338−8354.

(21) Pearton, S. J.; Yang, J.; Cary, P. H.; Ren, F.; Kim, J.; Tadjer, M. J.; Mastro, M. A. A Review of Ga 2 O 3 Materials, Processing, and Devices. *Appl. Phys. Rev.* **2018**, *5* (1), No. 011301.

(22) Higashiwaki, M.; Jessen, G. H. Guest Editorial: The Dawn of Gallium Oxide Microelectronics. *Appl. Phys. Lett.* **2018**, *112* (6), No. 060401.

(23) Higashiwaki, M.; Sasaki, K.; Kuramata, A.; Masui, T.; Yamakoshi, S. Gallium Oxide (Ga 2 O 3) Metal-Semiconductor Field-Effect Transistors on Single-Crystal β-Ga 2 O 3 (010) Substrates. *Appl. Phys. Lett.* **2012**, *100* (1), No. 013504.

(24) Green, A. J.; Speck, J.; Xing, G.; Moens, P.; Allerstam, F.; Gumaelius, K.; Neyer, T.; Arias-Purdue, A.; Mehrotra, V.; Kuramata, A.; Sasaki, K.; Watanabe, S.; Koshi, K.; Blevins, J.; Bierwagen, O.; Krishnamoorthy, S.; Leedy, K.; Arehart, A. R.; Neal, A. T.; Mou, S.; Ringel, S. A.; Kumar, A.; Sharma, A.; Ghosh, K.; Singisetti, U.; Li, W.; Chabak, K.; Liddy, K.; Islam, A.; Rajan, S.; Graham, S.; Choi, S.; Cheng, Z.; Higashiwaki, M. β-Gallium Oxide Power Electronics. *APL Mater.* **2022**, *10* (2), No. 029201.

(25) Geis, M. W.; Wade, T. C.; Wuorio, C. H.; Fedynyshyn, T. H.; Duncan, B.; Plaut, M. E.; Varghese, J. O.; Warnock, S. M.; Vitale, S. A.; Hollis, M. A. Progress Toward Diamond Power Field-Effect Transistors. *physica status solidi (a)* **2018**, *215* (22), No. 1800681.

(26) Ahmad, H.; Lindemuth, J.; Engel, Z.; Matthews, C. M.; McCrone, T. M.; Doolittle, W. A. Substantial P-Type Conductivity of AlN Achieved via Beryllium Doping. *Adv. Mater.* **2021**, *33* (42), No. 2104497.

(27) Davis, R. F.; Kelner, G.; Shur, M.; Edmond, J. A.; Palmour, J. W. Thin Film Deposition and Microelectronic and Optoelectronic Device Fabrication and Characterization in Monocrystalline Alpha and Beta Silicon Carbide. *Proceedings of the IEEE* **1991**, *79* (5), 677−701.

(28) Klauk, H.; Halik, M.; Zschieschang, U.; Schmid, G.; Radlik, W.; Weber, W. High-Mobility Polymer Gate Dielectric Pentacene Thin Film Transistors. *J. Appl. Phys.* **2002**, *92* (9), 5259−5263.

(29) Alvarez-Escalante, G.; Page, R.; Hu, R.; Xing, H. G.; Jena, D.; Tian, Z. High Thermal Conductivity and Ultrahigh Thermal Boundary Conductance of Homoepitaxial AlN Thin Films. *APL Mater.* **2022**, *10* (1), No. 011115.

(30) Bryan, I.; Bryan, Z.; Mita, S.; Rice, A.; Tweedie, J.; Collazo, R.; Sitar, Z. Surface Kinetics in AlN Growth: A Universal Model for the Control of Surface Morphology in III-Nitrides. *J. Cryst. Growth* **2016**, *438*, 81−89.

(31) Song, Y.; Zhang, C.; Lundh, J. S.; Huang, H.-L.; Zheng, Y.; Zhang, Y.; Park, M.; Mirabito, T.; Beaucejour, R.; Chae, C.; McIlwaine, N.; Esteves, G.; Beechem, T. E.; Moe, C.; Dargis, R.;

Jones, J.; Leach, J. H.; Lavelle, R. M.; Snyder, D. W.; Maria, J.-P.; Olsson, R. H.; Redwing, J. M.; Ansari, A.; Hwang, J.; Wang, X.; Foley, B. M.; Trolier-McKinstry, S. E.; Choi, S. Growth-Microstructure-Thermal Property Relations in AlN Thin Films. *J. Appl. Phys.* **2022**, *132* (17), 175108.

(32) Bondokov, R. T.; Mueller, S. G.; Morgan, K. E.; Slack, G. A.; Schujman, S.; Wood, M. C.; Smart, J. A.; Schowalter, L. J. Large-Area AlN Substrates for Electronic Applications: An Industrial Perspective. *J. Cryst. Growth* **2008**, *310* (17), 4020−4026.

(33) Lu, P.; Collazo, R.; Dalmau, R. F.; Durkaya, G.; Dietz, N.; Raghothamachar, B.; Dudley, M.; Sitar, Z. Seeded Growth of AlN Bulk Crystals in M- and c-Orientation. *J. Cryst. Growth* **2009**, *312* (1), 58−63.

(34) Xu, R. L.; Muñoz Rojo, M.; Islam, S. M.; Sood, A.; Vareskic, B.; Katre, A.; Mingo, N.; Goodson, K. E.; Xing, H. G.; Jena, D.; Pop, E. Thermal Conductivity of Crystalline AlN and the Influence of Atomic-Scale Defects. *J. Appl. Phys.* **2019**, *126* (18), 185105.

(35) Abeles, B.; Beers, D.; Cody, G.; Dismukes, J. Thermal Conductivity of Ge-Si Alloys at High Temperatures. *Physical review* **1962**, *125* (1), 44−46.

(36) Glassbrenner, C.; Slack, G. Thermal Conductivity of Silicon and Germanium from 3 K to the Melting Point. *Phys. Rev.* **1964**, *134*, A1058.

(37) Jezowski, A.; Stachowiak, P.; Plackowski, T.; Suski, T.; Krukowski, S.; Boćkowski, M.; Grzegory, I.; Danilchenko, B.; Paszkiewicz, T. Thermal Conductivity of GaN Crystals Grown by High Pressure Method. *Phys. Status Solidi B Basic Res.* **2003**, *240* (2), 447−450.

(38) Qian, X.; Jiang, P.; Yang, R. Anisotropic Thermal Conductivity of 4H and 6H Silicon Carbide Measured Using Time-Domain Thermoreflectance. *Materials Today Physics* **2017**, *3*, 70−75.

(39) Guo, Z.; Verma, A.; Wu, X.; Sun, F.; Hickman, A.; Masui, T.; Kuramata, A.; Higashiwaki, M.; Jena, D.; Luo, T. Anisotropic Thermal Conductivity in Single Crystal β-Gallium Oxide. *Appl. Phys. Lett.* **2015**, *106* (11), 111909.

(40) Wei, L.; Kuo, P. K.; Thomas, R. L.; Anthony, T. R.; Banholzer, W. F. Thermal Conductivity of Isotopically Modified Single Crystal Diamond. *Phys. Rev. Lett.* **1993**, *70* (24), 3764−3767.

(41) Onn, D. G.; Witek, A.; Qiu, Y. Z.; Anthony, T. R.; Banholzer, W. F. Some Aspects of the Thermal Conductivity of Isotopically Enriched Diamond Single Crystals. *Phys. Rev. Lett.* **1992**, *68* (18), 2806−2809.

(42) Cheng, Z.; Koh, Y. R.; Mamun, A.; Shi, J.; Bai, T.; Huynh, K.; Yates, L.; Liu, Z.; Li, R.; Lee, E.; Liao, M. E.; Wang, Y.; Yu, H. M.; Kushimoto, M.; Luo, T.; Goorsky, M. S.; Hopkins, P. E.; Amano, H.; Khan, A.; Graham, S. Experimental Observation of High Intrinsic Thermal Conductivity of AlN. *Phys. Rev. Mater.* **2020**, *4* (4), No. 044602.

(43) Pelá, R. R.; Caetano, C.; Marques, M.; Ferreira, L. G.; Furthmüller, J.; Teles, L. K. Accurate Band Gaps of AlGaN, InGaN, and AlInN Alloys Calculations Based on LDA-1/2 Approach. *Appl. Phys. Lett.* **2011**, *98* (15), 151907.

(44) Chatterjee, B.; Armstrong, A. M.; Klein, B. A.; Bansal, A.; Seyf, H. R.; Talreja, D.; Pogrebnyakov, A.; Heller, E.; Gopalan, V.; Henry, A. S.; Redwing, J. M.; Lundh, J. S.; Foley, B.; Choi, S.; Song, Y.; Shoemaker, D.; Baca, A. G.; Kaplar, R. J.; Beechem, T. E.; Saltonstall, C.; Allerman, A. A. Interdependence of Electronic and Thermal Transport in AlxGa1-XN Channel HEMTs. *IEEE Electron Device Lett.* **2020**, *41* (3), 461−464.

(45) Lundh, J. S.; Chatterjee, B.; Song, Y.; Baca, A. G.; Kaplar, R. J.; Beechem, T. E.; Allerman, A. A.; Armstrong, A. M.; Klein, B. A.; Bansal, A.; Talreja, D.; Pogrebnyakov, A.; Heller, E.; Gopalan, V.; Redwing, J. M.; Foley, B. M.; Choi, S. Multidimensional Thermal Analysis of an Ultrawide Bandgap AlGaN Channel High Electron Mobility Transistor. *Appl. Phys. Lett.* **2019**, *115* (15), 153503.

(46) Liu, W.; Balandin, A. A. Thermal Conduction in AlxGa1−xN Alloys and Thin Films. *J. Appl. Phys.* **2005**, *97* (7), No. 073710.

(47) Daly, B. C.; Maris, H. J.; Nurmikko, A. v.; Kuball, M.; Han, J. Optical Pump-and-Probe Measurement of the Thermal Conductivity of Nitride Thin Films. *J. Appl. Phys.* **2002**, *92* (7), 3820−3824.

(48) Chen, K.; Song, B.; Ravichandran, N. K.; Zheng, Q.; Chen, X.; Lee, H.; Sun, H.; Li, S.; Udalamatta Gamage, G. A. G.; Tian, F.; Ding, Z.; Song, Q.; Rai, A.; Wu, H.; Koirala, P.; Schmidt, A. J.; Watanabe, K.; Lv, B.; Ren, Z.; Shi, L.; Cahill, D. G.; Taniguchi, T.; Broido, D.; Chen, G. Ultrahigh Thermal Conductivity in Isotope-Enriched Cubic Boron Nitride. *Science (1979)* **2020**, *367* (6477), 555−559.

(49) Bauer, J. Optical Properties, Band Gap, and Surface Roughness of Si3N4. *Physica Status Solidi (a)* **1977**, *39* (2), 411−418.

(50) Kang, J. S.; Li, M.; Wu, H.; Nguyen, H.; Hu, Y. Experimental Observation of High Thermal Conductivity in Boron Arsenide. *Science (1979)* **2018**, *361* (6402), 575−578.

(51) Zhang, N.; Yu, X.; Pradhan, A.; Puppala, A. J. Thermal Conductivity of Quartz Sands by Thermo-Time Domain Reflectometry Probe and Model Prediction. *Journal of Materials in Civil Engineering* **2015**, *27* (12), No. 04015059.

(52) Gu, X.; Lee, C.; Xie, J.; Beam, E.; Becker, M.; Grotjohn, T. A.; Anaya, J.; Kuball, M.; Road, W. R. *GaN-on-Diamond with Ultra-Low Thermal Barrier Resistance GaN-on-Diamond preparation and surface morphology Thermal characterizations*; DoD, 2016; pp 405−408.

(53) Malakoutian, M.; Field, D. E.; Hines, N. J.; Pasayat, S.; Graham, S.; Kuball, M.; Chowdhury, S. Record-Low Thermal Boundary Resistance between Diamond and GaN-on-SiC for Enabling Radiofrequency Device Cooling. *ACS Appl. Mater. Interfaces* **2021**, *13* (50), 60553−60560.

(54) Cho, J.; Li, Y.; Altman, D. H.; Hoke, W. E.; Asheghi, M.; Goodson, K. E. Temperature Dependent Thermal Resistances at GaN-Substrate Interfaces in GaN Composite Substrates. In *Technical Digest - IEEE Compound Semiconductor Integrated Circuit Symposium, CSIC*, October 14−17, 2012, La Jolla, CA; IEEE, 2012; pp 5−8.

(55) Mu, F.; Cheng, Z.; Shi, J.; Shin, S.; Xu, B.; Shiomi, J.; Graham, S.; Suga, T. High Thermal Boundary Conductance across Bonded Heterogeneous GaN-SiC Interfaces. *ACS Appl. Mater. Interfaces* **2019**, *11* (36), 33428−33434.

(56) Bao, W.; Wang, Z.; Tang, D. Phonon Transport across GaN/AlN Interface: Interfacial Phonon Modes and Phonon Local Non-Equilibrium Analysis. *Int. J. Heat Mass Transf* **2022**, *183*, No. 122090.

(57) Wang, Z.; Sun, M.; Yao, G.; Tang, D.; Xu, K. Reconstruction of Thermal Boundary Resistance and Intrinsic Thermal Conductivity of SiO2-GaN-Sapphire Structure and Temperature Dependence. *International Journal of Thermal Sciences* **2015**, *87*, 178−186.

(58) Donovan, B. F.; Szwejkowski, C. J.; Duda, J. C.; Cheaito, R.; Gaskins, J. T.; Peter Yang, C. Y.; Constantin, C.; Jones, R. E.; Hopkins, P. E. Thermal Boundary Conductance across Metal-Gallium Nitride Interfaces from 80 to 450K. *Appl. Phys. Lett.* **2014**, *105* (20), 203502.

(59) Cheng, Z.; Bai, T.; Shi, J.; Feng, T.; Wang, Y.; Mecklenburg, M.; Li, C.; Hobart, K. D.; Feygelson, T. I.; Tadjer, M. J.; Pate, B. B.; Foley, B. M.; Yates, L.; Pantelides, S. T.; Cola, B. A.; Goorsky, M.; Graham, S. Tunable Thermal Energy Transport across Diamond Membranes and Diamond-Si Interfaces by Nanoscale Graphoepitaxy. *ACS Appl. Mater. Interfaces* **2019**, *11* (20), 18517−18527.

(60) Cheng, Z.; Wheeler, V. D.; Bai, T.; Shi, J.; Tadjer, M. J.; Feygelson, T.; Hobart, K. D.; Goorsky, M. S.; Graham, S. Integration of Polycrystalline Ga2O3 on Diamond for Thermal Management. *Appl. Phys. Lett.* **2020**, *116* (6), No. 062105.

(61) Cheng, Z.; Mu, F.; You, T.; Xu, W.; Shi, J.; Liao, M. E.; Wang, Y.; Huynh, K.; Suga, T.; Goorsky, M. S.; Ou, X.; Graham, S. Thermal Transport across Ion-Cut Monocrystalline β-Ga2O3 Thin Films and Bonded β-Ga2O3 − SiC Interfaces. *ACS Appl. Mater. Interfaces* **2020**, *12* (40), 44943−44951.

(62) Kim, S. H.; Shoemaker, D.; Green, A. J.; Chabak, K. D.; Liddy, K. J.; Graham, S.; Choi, S. Transient Thermal Management of a < inline-Formula> < tex-Math Notation = "LaTeX">β</Tex-Math> < /Inline-Formula>-Ga < inline-Formula> < tex-Math Notation = "LaTeX">$_{\text{2}}$</Tex-Math> < /Inline-Formula

> O < inline-Formula> < tex-Math Notation = ″LaTeX″>$_{\tex. *IEEE Trans. Electron Devices* **2023**, *70* (4), 1628−1635.

(63) Shi, J.; Yuan, C.; Huang, H.-L.; Johnson, J.; Chae, C.; Wang, S.; Hanus, R.; Kim, S.; Cheng, Z.; Hwang, J.; Graham, S. Thermal Transport across Metal/β-Ga 2 O 3 Interfaces. *ACS Appl. Mater. Interfaces* **2021**, *13* (24), 29083−29091.

(64) Wang, G.; Zhou, Y. Thermal Management Modeling for β-Ga2O3-Highly Thermal Conductive Substrates Heterostructures. *IEEE Trans Compon Packaging Manuf Technol.* **2022**, *12* (4), 638−646.

(65) Yuan, C.; Zhang, Y.; Montgomery, R.; Kim, S.; Shi, J.; Mauze, A.; Itoh, T.; Speck, J. S.; Graham, S. Modeling and Analysis for Thermal Management in Gallium Oxide Field-Effect Transistors. *J. Appl. Phys.* **2020**, *127* (15), 154502.

(66) Cheng, Z.; Yates, L.; Shi, J.; Tadjer, M. J.; Hobart, K. D.; Graham, S. Thermal Conductance across β-Ga2O3-Diamond van Der Waals Heterogeneous Interfaces. *APL Mater.* **2019**, *7* (3), No. 031118.

(67) Cheng, Z.; Graham, S.; Amano, H.; Cahill, D. G. Perspective on Thermal Conductance across Heterogeneously Integrated Interfaces for Wide and Ultrawide Bandgap Electronics. *Appl. Phys. Lett.* **2022**, *120* (3), No. 030501.

(68) Chatterjee, B.; Zeng, K.; Nordquist, C. D.; Singisetti, U.; Choi, S. Device-Level Thermal Management of Gallium Oxide Field-Effect Transistors. *IEEE Trans Compon Packaging Manuf Technol.* **2019**, *9* (12), 2352−2365.

(69) Hopkins, P. E. Thermal Transport across Solid Interfaces with Nanoscale Imperfections: Effects of Roughness, Disorder, Dislocations, and Bonding on Thermal Boundary Conductance. *ISRN Mechanical Engineering* **2013**, *2013* (1), No. 682586.

(70) Monachon, C.; Weber, L.; Dames, C. Thermal Boundary Conductance: A Materials Science Perspective. *Annu. Rev. Mater. Res.* **2016**, *46* (1), 433−463.

(71) Giri, A.; Hopkins, P. E. A Review of Experimental and Computational Advances in Thermal Boundary Conductance and Nanoscale Thermal Transport across Solid Interfaces. *Adv. Funct Mater.* **2020**, *30* (8), No. 1903857.

(72) Chen, J.; Xu, X.; Zhou, J.; Li, B. Interfacial Thermal Resistance: Past, Present, and Future. *Rev. Mod. Phys.* **2022**, *94* (2), No. 025002.

(73) Xie, R.; Tiwari, J.; Feng, T. Impacts of Various Interfacial Nanostructures on Spectral Phonon Thermal Boundary Conductance. *J. Appl. Phys.* **2022**, *132* (11), 115108.

(74) Cheng, Z.; Li, R.; Yan, X.; Jernigan, G.; Shi, J.; Liao, M. E.; Hines, N. J.; Gadre, C. A.; Idrobo, J. C.; Lee, E.; Hobart, K. D.; Goorsky, M. S.; Pan, X.; Luo, T.; Graham, S. Experimental Observation of Localized Interfacial Phonon Modes. *Nat. Commun.* **2021**, *12* (1), 6901.

(75) Tian, Z.; Esfarjani, K.; Chen, G. Enhancing Phonon Transmission across a Si/Ge Interface by Atomic Roughness: First-Principles Study with the Green's Function Method. *Phys. Rev. B* **2012**, *86* (23), No. 235304.

(76) Cheng, Z.; Bai, T.; Shi, J.; Feng, T.; Wang, Y.; Mecklenburg, M.; Li, C.; Hobart, K. D.; Feygelson, T. I.; Tadjer, M. J.; Pate, B. B.; Foley, B. M.; Yates, L.; Pantelides, S. T.; Cola, B. A.; Goorsky, M.; Graham, S. Tunable Thermal Energy Transport across Diamond Membranes and Diamond-Si Interfaces by Nanoscale Graphoepitaxy. *ACS Appl. Mater. Interfaces* **2019**, *11* (20), 18517−18527.

(77) Xu, Y.; Wang, G.; Zhou, Y. Broadly Manipulating the Interfacial Thermal Energy Transport across the Si/4H-SiC Interfaces via Nanopatterns. *Int. J. Heat Mass Transf* **2022**, *187*, No. 122499.

(78) Cho, J.; Li, Y.; Altman, D. H.; Hoke, W. E.; Asheghi, M.; Goodson, K. E. Temperature Dependent Thermal Resistances at GaN-Substrate Interfaces in GaN Composite Substrates. In *Technical Digest - IEEE Compound Semiconductor Integrated Circuit Symposium, CSIC*, October 14−17, 2012, La Jolla, CA; IEEE, 2012; pp 5−8.

(79) Cho, J.; Li, Y.; Hoke, W. E.; Altman, D. H.; Asheghi, M.; Goodson, K. E. Phonon Scattering in Strained Transition Layers for GaN Heteroepitaxy. *Phys. Rev. B* **2014**, *89* (11), No. 115301.

(80) Ziade, E.; Yang, J.; Brummer, G.; Nothern, D.; Moustakas, T.; Schmidt, A. J. Thermal Transport through GaN−SiC Interfaces from 300 to 600 K. *Appl. Phys. Lett.* **2015**, *107* (9), No. 091605.

(81) Koh, Y. R.; Hoque, M. S. B.; Ahmad, H.; Olson, D. H.; Liu, Z.; Shi, J.; Wang, Y.; Huynh, K.; Hoglund, E. R.; Aryana, K.; Howe, J. M.; Goorsky, M. S.; Graham, S.; Luo, T.; Hite, J. K.; Doolittle, W. A.; Hopkins, P. E. High Thermal Conductivity and Thermal Boundary Conductance of Homoepitaxially Grown Gallium Nitride (GaN) Thin Films. *Phys. Rev. Mater.* **2021**, *5* (10), No. 104604.

(82) Cheng, Z.; Wheeler, V. D.; Bai, T.; Shi, J.; Tadjer, M. J.; Feygelson, T.; Hobart, K. D.; Goorsky, M. S.; Graham, S. Integration of Polycrystalline Ga2O3 on Diamond for Thermal Management. *Appl. Phys. Lett.* **2020**, *116* (6), No. 062105.

(83) Yang, S.; Song, H.; Peng, Y.; Zhao, L.; Tong, Y.; Kang, F.; Xu, M.; Sun, B.; Wang, X. Reduced Thermal Boundary Conductance in GaN-Based Electronic Devices Introduced by Metal Bonding Layer. *Nano Res.* **2021**, *14* (10), 3616−3620.

(84) Waller, W. M.; Pomeroy, J. W.; Field, D.; Smith, E. J. W.; May, P. W.; Kuball, M. Thermal Boundary Resistance of Direct van Der Waals Bonded GaN-on-Diamond. *Semicond. Sci. Technol.* **2020**, *35* (9), No. 095021.

(85) Yates, L.; Anderson, J.; Gu, X.; Lee, C.; Bai, T.; Mecklenburg, M.; Aoki, T.; Goorsky, M. S.; Kuball, M.; Piner, E. L.; Graham, S. Low Thermal Boundary Resistance Interfaces for GaN-on-Diamond Devices. *ACS Appl. Mater. Interfaces* **2018**, *10* (28), 24302−24309.

(86) Zhou, Y.; Anaya, J.; Pomeroy, J.; Sun, H.; Gu, X.; Xie, A.; Beam, E.; Becker, M.; Grotjohn, T. A.; Lee, C.; Kuball, M. Barrier-Layer Optimization for Enhanced GaN-on-Diamond Device Cooling. *ACS Appl. Mater. Interfaces* **2017**, *9* (39), 34416−34422.

(87) Cho, J.; Won, Y.; Francis, D.; Asheghi, M.; Goodson, K. E. Thermal Interface Resistance Measurements for GaN-on-Diamond Composite Substrates. In *2014 IEEE Compound Semiconductor Integrated Circuit Symposium (CSICS)*, October 19−22, 2014, La Jolla, CA; IEEE, 2014; pp 1−4.

(88) Pomeroy, J. W.; Simon, R. B.; Sun, H.; Francis, D.; Faili, F.; Twitchen, D. J.; Kuball, M. Contactless Thermal Boundary Resistance Measurement of GaN-on-Diamond Wafers. *IEEE Electron Device Lett.* **2014**, *35* (10), 1007−1009.

(89) Pomeroy, J. W.; Bernardoni, M.; Dumka, D. C.; Fanning, D. M.; Kuball, M. Low Thermal Resistance GaN-on-Diamond Transistors Characterized by Three-Dimensional Raman Thermography Mapping. *Appl. Phys. Lett.* **2014**, *104* (8), No. 083513.

(90) Sun, H.; Simon, R. B.; Pomeroy, J. W.; Francis, D.; Faili, F.; Twitchen, D. J.; Kuball, M. Reducing GaN-on-Diamond Interfacial Thermal Resistance for High Power Transistor Applications. *Appl. Phys. Lett.* **2015**, *106* (11), 111906.

(91) Altman, D.; Tyhach, M.; McClymonds, J.; Kim, S.; Graham, S.; Cho, J.; Goodson, K.; Francis, D.; Faili, F.; Ejeckam, F.; Bernstein, S. Analysis and Characterization of Thermal Transport in GaN HEMTs on Diamond Substrates. In *Thermomechanical Phenomena in Electronic Systems -Proceedings of the Intersociety Conference*, May 27−30, 2014; IEEE, 2014; pp 1199−1205.

(92) Dumka, D. C.; Chou, T. M.; Jimenez, J. L.; Fanning, D. M.; Francis, D.; Faili, F.; Ejeckam, F.; Bernardoni, M.; Pomeroy, J. W.; Kuball, M. Electrical and Thermal Performance of AlGaN/GaN HEMTs on Diamond Substrate for RF Applications. In *2013 IEEE Compound Semiconductor Integrated Circuit Symposium (CSICS)*, October 13−16, 2013; IEEE, 2013; pp 1−4.

(93) Goyal, V.; Kotchetkov, D.; Subrina, S.; Rahman, M.; Balandin, A. A. Thermal Conduction through Diamond - Silicon Heterostructures. In *2010 12th IEEE Intersociety Conference on Thermal and Thermomechanical Phenomena in Electronic Systems*, June 2−5, 2010, Las Vegas, NV; IEEE, 2010; pp 1−6.

(94) Goyal, V.; Subrina, S.; Nika, D. L.; Balandin, A. A. Reduced Thermal Resistance of the Silicon-Synthetic Diamond Composite Substrates at Elevated Temperatures. *Appl. Phys. Lett.* **2010**, *97* (3), No. 031904.

(95) Goodson, K. E.; Käding, O. W.; Rösler, M.; Zachai, R. Experimental Investigation of Thermal Conduction Normal to Diamond-Silicon Boundaries. *J. Appl. Phys.* **1995**, 77 (4), 1385−1392.
(96) Goodson, K. E.; Käding, O. W.; Rösner, M.; Zachai, R. Thermal Conduction Normal to Diamond-silicon Boundaries. *Appl. Phys. Lett.* **1995**, *66* (23), 3134−3136.
(97) Klokov, A. Y.; Aminev, D. F.; Sharkov, A. I.; Galkina, T. I.; Ralchenko, V. G. Evaluation of Thermal Parameters of Layers and Interfaces in Silicon-on-Diamond Structures by a Photothermal Method. *J. Phys. Conf Ser.* **2010**, *214*, No. 012108.
(98) Mohr, M.; Daccache, L.; Horvat, S.; Brühne, K.; Jacob, T.; Fecht, H.-J. J. Influence of Grain Boundaries on Elasticity and Thermal Conductivity of Nanocrystalline Diamond Films. *Acta Mater.* **2017**, *122*, 92−98.
(99) Malakoutian, M.; Field, D. E.; Hines, N. J.; Pasayat, S.; Graham, S.; Kuball, M.; Chowdhury, S. Record-Low Thermal Boundary Resistance between Diamond and GaN-on-SiC for Enabling Radiofrequency Device Cooling. *ACS Appl. Mater. Interfaces* **2021**, *13* (50), 60553−60560.
(100) Yates, L.; Bougher, T. L.; Beechem, T.; Cola, B. A.; Graham, S. The Impact of Interfacial Layers on the Thermal Boundary Resistance and Residual Stress in GaN on Si Epitaxial Layers. In *Advanced Fabrication and Manufacturing; Emerging Technology Frontiers; Energy, Health and Water- Applications of Nano-, Micro- and Mini-Scale Devices; MEMS and NEMS; Technology Update Talks; Thermal Management Using Micro Channels, Jets, Sprays*; American Society of Mechanical Engineers, 2015; pp 1−8, Vol. *3*.
(101) Kang, J. S.; Li, M.; Wu, H.; Nguyen, H.; Aoki, T.; Hu, Y. Integration of Boron Arsenide Cooling Substrates into Gallium Nitride Devices. *Nat. Electron* **2021**, *4* (6), 416−423.
(102) Field, D. E.; Pomeroy, J. W.; Gity, F.; Schmidt, M.; Torchia, P.; Li, F.; Gammon, P. M.; Shah, V. A.; Kuball, M. Thermal Characterization of Direct Wafer Bonded Si-on-SiC. *Appl. Phys. Lett.* **2022**, *120* (11), 113503.
(103) Matsumae, T.; Kurashima, Y.; Umezawa, H.; Tanaka, K.; Ito, T.; Watanabe, H.; Takagi, H. Low-Temperature Direct Bonding of *β*-Ga 2 O 3 and Diamond Substrates under Atmospheric Conditions. *Appl. Phys. Lett.* **2020**, *116* (14), 141602.
(104) Cheng, Z.; Mu, F.; Yates, L.; Suga, T.; Graham, S. Interfacial Thermal Conductance across Room-Temperature-Bonded GaN/Diamond Interfaces for GaN-on-Diamond Devices. *ACS Appl. Mater. Interfaces* **2020**, *12* (7), 8376−8384.
(105) Mu, F.; Xu, B.; Wang, X.; Gao, R.; Huang, S.; Wei, K.; Takeuchi, K.; Chen, X.; Yin, H.; Wang, D.; Yu, J.; Suga, T.; Shiomi, J.; Liu, X. A Novel Strategy for GaN-on-Diamond Device with a High Thermal Boundary Conductance. *arXiv (Applied Physics)*, 2107.10473, ver. 1. https://arxiv.org/abs/2107.10473 (accessed 6/13/2023).
(106) Mu, F.; Cheng, Z.; Shi, J.; Shin, S.; Xu, B.; Shiomi, J.; Graham, S.; Suga, T. High Thermal Boundary Conductance across Bonded Heterogeneous GaN-SiC Interfaces. *ACS Appl. Mater. Interfaces* **2019**, *11* (36), 33428−33434.
(107) Xu, Y.; Mu, F.; Wang, Y.; Chen, D.; Ou, X.; Suga, T. Direct Wafer Bonding of Ga2O3−SiC at Room Temperature. *Ceram. Int.* **2019**, *45* (5), 6552−6555.
(108) Cho, J.; Li, Z.; Bozorg-Grayeli, E.; Kodama, T.; Francis, D.; Ejeckam, F.; Faili, F.; Asheghi, M.; Goodson, K. E. Improved Thermal Interfaces of GaN-Diamond Composite Substrates for HEMT Applications. *IEEE Trans Compon Packaging Manuf Technol.* **2013**, *3* (1), 79−85.
(109) Cho, J.; Francis, D.; Altman, D. H.; Asheghi, M.; Goodson, K. E. Phonon Conduction in GaN-Diamond Composite Substrates. *J. Appl. Phys.* **2017**, *121* (5), No. 055105.
(110) Cahill, D. G. Analysis of Heat Flow in Layered Structures for Time-Domain Thermoreflectance. *Rev. Sci. Instrum.* **2004**, *75* (12), 5119−5122.
(111) Schmidt, A. J.; Cheaito, R.; Chiesa, M. A Frequency-Domain Thermoreflectance Method for the Characterization of Thermal Properties. *Rev. Sci. Instrum.* **2009**, *80* (9), No. 094901.
(112) Kuzmík, J.; Bychikhin, S.; Pogany, D.; Gaquière, C.; Pichonat, E.; Morvan, E. Investigation of the Thermal Boundary Resistance at the III-Nitride/Substrate Interface Using Optical Methods. *J. Appl. Phys.* **2007**, *101* (5), No. 054508.
(113) Liu, K.; Zhao, J.; Sun, H.; Guo, H.; Dai, B.; Zhu, J. Thermal Characterization of GaN Heteroepitaxies Using Ultraviolet Transient Thermoreflectance. *Chinese Physics B* **2019**, *28* (6), No. 060701.
(114) Stevens, R. J.; Smith, A. N.; Norris, P. M. Measurement of Thermal Boundary Conductance of a Series of Metal-Dielectric Interfaces by the Transient Thermoreflectance Technique. *J. Heat Transfer* **2005**, *127* (3), 315−322.
(115) Little, W. A. THE TRANSPORT OF HEAT BETWEEN DISSIMILAR SOLIDS AT LOW TEMPERATURES. *Can. J. Phys.* **1959**, *37* (3), 334−349.
(116) Swartz, E. T.; Pohl, R. O. Thermal Resistance at Interfaces. *Appl. Phys. Lett.* **1987**, *51* (26), 2200−2202.
(117) Swartz, E.; Pohl, R. Thermal Boundary Resistance. *Rev. Mod. Phys.* **1989**, *61* (3), 605−668.
(118) Zhang, W.; Mingo, N.; Fisher, T. Simulation of Phonon Transport across a Non-Polar Nanowire Junction Using an Atomistic Green's Function Method. *Phys. Rev. B* **2007**, *76* (19), No. 195429.
(119) Zhang, W.; Fisher, T. S.; Mingo, N. Simulation of Interfacial Phonon Transport in Si−Ge Heterostructures Using an Atomistic Green's Function Method. *J. Heat Transfer* **2007**, *129* (4), 483.
(120) Mingo, N.; Yang, L. Phonon Transport in Nanowires Coated with an Amorphous Material: An Atomistic Green's Function Approach. *Phys. Rev. B* **2003**, *68* (24), No. 245406.
(121) Hopkins, P. E.; Norris, P. M. Effects of Joint Vibrational States on Thermal Boundary Conductance. *Nanoscale and Microscale Thermophysical Engineering* **2007**, *11* (3−4), 247−257.
(122) Hopkins, P. E.; Norris, P. M. Relative Contributions of Inelastic and Elastic Diffuse Phonon Scattering to Thermal Boundary Conductance across Solid Interfaces. *J. Heat Transfer* **2009**, *131* (2), No. 022402.
(123) Hopkins, P. E.; Duda, J. C.; Norris, P. M. Anharmonic Phonon Interactions at Interfaces and Contributions to Thermal Boundary Conductance. *J. Heat Transfer* **2011**, *133* (6), No. 062401.
(124) Prasher, R.; Hu, X.; Chalopin, Y.; Mingo, N.; Lofgreen, K.; Volz, S.; Cleri, F.; Keblinski, P. Turning Carbon Nanotubes from Exceptional Heat Conductors into Insulators. *Phys. Rev. Lett.* **2009**, *102* (10), No. 105901.
(125) Reddy, P.; Castelino, K.; Majumdar, A. Diffuse Mismatch Model of Thermal Boundary Conductance Using Exact Phonon Dispersion. *Appl. Phys. Lett.* **2005**, *87* (21), 211908.
(126) Sadasivam, S.; Ye, N.; Feser, J. P.; Charles, J.; Miao, K.; Kubis, T.; Fisher, T. S. Thermal Transport across Metal Silicide-Silicon Interfaces: First-Principles Calculations and Green's Function Transport Simulations. *Phys. Rev. B* **2017**, *95* (8), No. 085310.
(127) *Thermal Nanosystems and Nanomaterials*; Volz, S., Ed.; Topics in Applied Physics; Springer Berlin Heidelberg: Berlin, Heidelberg, 2009; Vol. *118*.
(128) Shin, S.; Kaviany, M.; Desai, T.; Bonner, R. Roles of Atomic Restructuring in Interfacial Phonon Transport. *Phys. Rev. B* **2010**, *82* (8), No. 081302.
(129) Dai, J.; Tian, Z. Rigorous Formalism of Anharmonic Atomistic Green's Function for Three-Dimensional Interfaces. *Phys. Rev. B* **2020**, *101* (4), No. 41301.
(130) Schelling, P. K.; Phillpot, S. R.; Keblinski, P. Kapitza Conductance and Phonon Scattering at Grain Boundaries by Simulation. *J. Appl. Phys.* **2004**, *95* (11), 6082−6091.
(131) Shi, J.; Lee, J.; Dong, Y.; Roy, A.; Fisher, T. S.; Ruan, X. Dominant Phonon Polarization Conversion across Dimensionally Mismatched Interfaces: Carbon-Nanotube−Graphene Junction. *Phys. Rev. B* **2018**, *97* (13), No. 134309.
(132) Roberts, N. A.; Walker, D. G. Phonon Wave-Packet Simulations of Ar/Kr Interfaces for Thermal Rectification. *J. Appl. Phys.* **2010**, *108* (12), 123515.

(133) Baker, C. H.; Jordan, D. A.; Norris, P. M. Application of the Wavelet Transform to Nanoscale Thermal Transport. *Phys. Rev. B* **2012**, *86* (10), No. 104306.
(134) Schelling, P. K.; Phillpot, S. R.; Keblinski, P. Phonon Wave-Packet Dynamics at Semiconductor Interfaces by Molecular-Dynamics Simulation. *Appl. Phys. Lett.* **2002**, *80* (14), 2484.
(135) Feng, T.; Zhong, Y.; Shi, J.; Ruan, X. Unexpected High Inelastic Phonon Transport across Solid-Solid Interface: Modal Nonequilibrium Molecular Dynamics Simulations and Landauer Analysis. *Phys. Rev. B* **2019**, *99* (4), No. 045301.
(136) Chalopin, Y.; Volz, S. A Microscopic Formulation of the Phonon Transmission at the Nanoscale. *Appl. Phys. Lett.* **2013**, *103* (5), No. 051602.
(137) Sääskilahti, K.; Oksanen, J.; Tulkki, J.; Volz, S. Role of Inelastic Phonon Scattering in the Spectrally Decomposed Thermal Conductance at Interfaces. *Phys. Rev. B* **2014**, *90* (13), No. 134312.
(138) Sääskilahti, K.; Oksanen, J.; Tulkki, J.; Volz, S. Spectral Mapping of Heat Transfer Mechanisms at Liquid-Solid Interfaces. *Phys. Rev. E* **2016**, *93* (5), No. 052141.
(139) Zhou, Y.; Hu, M. Full Quantification of Frequency-Dependent Interfacial Thermal Conductance Contributed by Two- and Three-Phonon Scattering Processes from Nonequilibrium Molecular Dynamics Simulations. *Phys. Rev. B* **2017**, *95* (11), No. 115313.
(140) Murakami, T.; Hori, T.; Shiga, T.; Shiomi, J. Probing and Tuning Inelastic Phonon Conductance across Finite-Thickness Interface. *Applied Physics Express* **2014**, *7* (12), No. 121801.
(141) Giri, A.; Braun, J. L.; Hopkins, P. E. Implications of Interfacial Bond Strength on the Spectral Contributions to Thermal Boundary Conductance across Solid, Liquid, and Gas Interfaces: A Molecular Dynamics Study. *J. Phys. Chem. C* **2016**, *120* (43), 24847−24856.
(142) Gordiz, K.; Henry, A. A Formalism for Calculating the Modal Contributions to Thermal Interface Conductance. *New J. Phys.* **2015**, *17* (10), No. 103002.
(143) Gordiz, K.; Henry, A. Phonon Transport at Interfaces: Determining the Correct Modes of Vibration. *J. Appl. Phys.* **2016**, *119* (1), No. 015101.
(144) Gordiz, K.; Henry, A. Phonon Transport at Crystalline Si/Ge Interfaces: The Role of Interfacial Modes of Vibration. *Sci. Rep* **2016**, *6*, 23139.
(145) Kuzmik, J.; Bychikhin, S.; Pogany, D.; Pichonat, E.; Lancry, O.; Gaquière, C.; Tsiakatouras, G.; Deligeorgis, G.; Georgakilas, A. Thermal Characterization of MBE-Grown GaN/AlGaN/GaN Device on Single Crystalline Diamond. *J. Appl. Phys.* **2011**, *109* (8), No. 086106.
(146) Pomeroy, J.; Bernardoni, M.; Sarua, A.; Manoi, A.; Dumka, D. C.; Fanning, D. M.; Kuball, M. Achieving the Best Thermal Performance for GaN-on-Diamond. In *2013 IEEE Compound Semiconductor Integrated Circuit Symposium (CSICS)*, October 13−16, 2013, Monterey, CA; IEEE, 2013; pp 1−4.
(147) Tao, L.; Sreenivasan, S. T.; Shahsavari, R. Interlaced, Nanostructured Interface with Graphene Buffer Layer Reduces Thermal Boundary Resistance in Nano/Microelectronic Systems. *ACS Appl. Mater. Interfaces* **2017**, *9* (1), 989−998.
(148) Cho, J.; Bozorg-Grayeli, E.; Altman, D. H.; Asheghi, M.; Goodson, K. E. Low Thermal Resistances at GaN-SiC Interfaces for HEMT Technology. *IEEE Electron Device Lett.* **2012**, *33* (3), 378−380.
(149) Kuzmík, J.; Bychikhin, S.; Pogany, D.; Gaquière, C.; Pichonat, E.; Morvan, E. Investigation of the Thermal Boundary Resistance at the III-Nitride/Substrate Interface Using Optical Methods. *J. Appl. Phys.* **2007**, *101* (5), No. 054508.
(150) Hu, M.; Zhang, X.; Poulikakos, D.; Grigoropoulos, C. P. Large "near Junction" Thermal Resistance Reduction in Electronics by Interface Nanoengineering. *Int. J. Heat Mass Transf* **2011**, *54* (25−26), 5183−5191.
(151) Hu, M.; Poulikakos, D. Graphene Mediated Thermal Resistance Reduction at Strongly Coupled Interfaces. *Int. J. Heat Mass Transf* **2013**, *62* (1), 205−213.
(152) Lee, E.; Zhang, T.; Hu, M.; Luo, T. Thermal Boundary Conductance Enhancement Using Experimentally Achievable Nanostructured Interfaces-Analytical Study Combined with Molecular Dynamics Simulation. *Phys. Chem. Chem. Phys.* **2016**, *18* (25), 16794−16801.
(153) Lee, E.; Luo, T. The Role of Optical Phonons in Intermediate Layer-Mediated Thermal Transport across Solid Interfaces. *Phys. Chem. Chem. Phys.* **2017**, *19* (28), 18407−18415.
(154) Li, R.; Gordiz, K.; Henry, A.; Hopkins, P. E.; Lee, E.; Luo, T. Effect of Light Atoms on Thermal Transport across Solid-Solid Interfaces. *Phys. Chem. Chem. Phys.* **2019**, *21* (31), 17029−17035.
(155) Lee, E.; Luo, T. Thermal Transport across Solid-Solid Interfaces Enhanced by Pre-Interface Isotope-Phonon Scattering. *Appl. Phys. Lett.* **2018**, *112* (1), No. 011603.
(156) Koh, Y. K.; Cao, Y.; Cahill, D. G.; Jena, D. Heat-Transport Mechanisms in Superlattices. *Adv. Funct Mater.* **2009**, *19* (4), 610−615.
(157) Liang, Z.; Keblinski, P. Finite-Size Effects on Molecular Dynamics Interfacial Thermal-Resistance Predictions. *Phys. Rev. B* **2014**, *90*, No. 075411.
(158) Liang, Z.; Sasikumar, K.; Keblinski, P. Thermal Transport across a Substrate−Thin-Film Interface: Effects of Film Thickness and Surface Roughness. *Phys. Rev. Lett.* **2014**, *113* (6), No. 065901.
(159) Polanco, C. A.; Lindsay, L. Phonon Thermal Conductance across GaN-AlN Interfaces from First Principles. *Phys. Rev. B* **2019**, *99* (7), No. 075202.
(160) Wang, Q.; Wang, X.; Liu, X.; Zhang, J. Interfacial Engineering for the Enhancement of Interfacial Thermal Conductance in GaN/AlN Heterostructure. *J. Appl. Phys.* **2021**, *129* (23), 235102.
(161) Bao, W.; Wang, Z.; Tang, D. Phonon Transport across GaN/AlN Interface: Interfacial Phonon Modes and Phonon Local Non-Equilibrium Analysis. *Int. J. Heat Mass Transf* **2022**, *183*, No. 122090.
(162) Sun, J.; Li, Y.; Karaaslan, Y.; Sevik, C.; Chen, Y. Misfit Dislocation Structure and Thermal Boundary Conductance of GaN/AlN Interfaces. *J. Appl. Phys.* **2021**, *130* (3), No. 035301.
(163) Wang, Z.; Tian, X.; Liang, J.; Zhu, J.; Tang, D.; Xu, K. Prediction and Measurement of Thermal Transport across Interfaces between Semiconductor and Adjacent Layers. *International Journal of Thermal Sciences* **2014**, *79*, 266−275.
(164) Wang, Z.; Sun, M.; Yao, G.; Tang, D.; Xu, K. Reconstruction of Thermal Boundary Resistance and Intrinsic Thermal Conductivity of SiO2-GaN-Sapphire Structure and Temperature Dependence. *International Journal of Thermal Sciences* **2015**, *87*, 178−186.
(165) Gaskins, J. T.; Kotsonis, G.; Giri, A.; Ju, S.; Rohskopf, A.; Wang, Y.; Bai, T.; Sachet, E.; Shelton, C. T.; Liu, Z.; Cheng, Z.; Foley, B. M.; Graham, S.; Luo, T.; Henry, A.; Goorsky, M. S.; Shiomi, J.; Maria, J. P.; Hopkins, P. E. Thermal Boundary Conductance Across Heteroepitaxial ZnO/GaN Interfaces: Assessment of the Phonon Gas Model. *Nano Lett.* **2018**, *18* (12), 7469−7477.
(166) Freedman, J. P.; Leach, J. H.; Preble, E. A.; Sitar, Z.; Davis, R. F.; Malen, J. A. Universal Phonon Mean Free Path Spectra in Crystalline Semiconductors at High Temperature. *Sci. Rep* **2013**, *3* (1), 2963.
(167) Jones, R. E.; Duda, J. C.; Zhou, X. W.; Kimmer, C. J.; Hopkins, P. E. Investigation of Size and Electronic Effects on Kapitza Conductance with Non-Equilibrium Molecular Dynamics. *Appl. Phys. Lett.* **2013**, *102* (18), 183119.
(168) Zhou, X. W.; Jones, R. E.; Kimmer, C. J.; Duda, J. C.; Hopkins, P. E. Relationship of Thermal Boundary Conductance to Structure from an Analytical Model plus Molecular Dynamics Simulations. *Phys. Rev. B* **2013**, *87* (9), No. 094303.
(169) Zheng, Q.; Li, C.; Rai, A.; Leach, J. H.; Broido, D. A.; Cahill, D. G. Thermal Conductivity of GaN, GaN 71, and SiC from 150 to 850 K. *Phys. Rev. Mater.* **2019**, *3* (1), No. 014601.
(170) Schenk, A.; Tadich, A.; Sear, M.; O'Donnell, K. M.; Ley, L.; Stacey, A.; Pakes, C. Formation of a Silicon Terminated (100) Diamond Surface. *Appl. Phys. Lett.* **2015**, *106* (19), 191603.

https://doi.org/10.1021/acsami.3c02507
ACS Appl. Mater. Interfaces 2023, 15, 29655−29673

(171) Sear, M. J.; Schenk, A. K.; Tadich, A.; Stacey, A.; Pakes, C. I. P-Type Surface Transfer Doping of Oxidised Silicon Terminated (100) Diamond. *Appl. Phys. Lett.* **2017**, *110* (1), 011605.

(172) Goodson, K. E.; Käding, O. W.; Zachai, R.Thermal Resistances at the Boundaries of CVD Diamond Layers in Electronic Systems. In *Thermal Resistances at the Boundaries of CVD Diamond Layers in Electronic Systems*, November 7−11, 1994, Chicago, IL; ASME, 1994; Vol. *292*, p 83.

(173) Khosravian, N.; Samani, M. K.; Loh, G. C.; Chen, G. C. K. K.; Baillargeat, D.; Tay, B. K. Molecular Dynamic Simulation of Diamond/Silicon Interfacial Thermal Conductance. *J. Appl. Phys.* **2013**, *113* (2), No. 024907.

(174) Cheng, Z.; Liang, J.; Kawamura, K.; Asamura, H.; Uratani, H.; Graham, S.; Ohno, Y.; Nagai, Y.; Shigekawa, N.; Cahill, D. G. High Thermal Conductivity in Wafer Scale Cubic Silicon Carbide Crystals. *arXiv (Materials Science)*, 2022, 2207.05292, ver. 1. https://arxiv.org/abs/2207.05292 (accessed 6/13/2023).

(175) Cheng, Z.; Mu, F.; Ji, X.; You, T.; Xu, W.; Suga, T.; Ou, X.; Cahill, D. G.; Graham, S. Thermal Visualization of Buried Interfaces Enabled by Ratio Signal and Steady-State Heating of Time-Domain Thermoreflectance. *ACS Appl. Mater. Interfaces* **2021**, *13* (27), 31843−31851.

(176) Liang, J.; Nagai, H.; Cheng, Z.; Kawamura, K.; Shimizu, Y.; Ohno, Y. Selective Direct Bonding of High Thermal Conductivity 3C-SiC Film to β -Ga2O3 for Top-Side Heat Extraction. *arXiv (Materials Science)*, 2022, 2209.05669, ver. 1. https://arxiv.org/abs/2209.05669 (accessed 6/13/2023).

(177) Aller, H. T.; Yu, X.; Wise, A.; Howell, R. S.; Gellman, A. J.; McGaughey, A. J. H.; Malen, J. A. Chemical Reactions Impede Thermal Transport across Metal/β-Ga2O3 Interfaces. *Nano Lett.* **2019**, *19* (12), 8533−8538.

(178) Hanus, R.; Gurunathan, R.; Lindsay, L.; Agne, M. T.; Shi, J.; Graham, S.; Jeffrey Snyder, G. Thermal Transport in Defective and Disordered Materials. *Appl. Phys. Rev.* **2021**, *8* (3), No. 031311.

(179) Cheng, Z.; Koh, Y. R.; Ahmad, H.; Hu, R.; Shi, J.; Liao, M. E.; Wang, Y.; Bai, T.; Li, R.; Lee, E.; Clinton, E. A.; Matthews, C. M.; Engel, Z.; Yates, L.; Luo, T.; Goorsky, M. S.; Doolittle, W. A.; Tian, Z.; Hopkins, P. E.; Graham, S. Thermal Conductance across Harmonic-Matched Epitaxial Al-Sapphire Heterointerfaces. *Commun. Phys.* **2020**, *3* (1), 115.

(180) Ye, N.; Feser, J. P.; Sadasivam, S.; Fisher, T. S.; Wang, T.; Ni, C.; Janotti, A. Thermal Transport across Metal Silicide-Silicon Interfaces: An Experimental Comparison between Epitaxial and Nonepitaxial Interfaces. *Phys. Rev. B* **2017**, *95* (8), No. 085430.

https://doi.org/10.1021/acsami.3c02507
ACS Appl. Mater. Interfaces 2023, 15, 29655−29673

ACS APPLIED MATERIALS & INTERFACES

www.acsami.org Addition/Correction

Correction to "A Critical Review of Thermal Boundary Conductance across Wide and Ultrawide Bandgap Semiconductor Interfaces"

Tianli Feng,* Hao Zhou, Zhe Cheng, Leighann Sarah Larkin, and Mahesh R. Neupane

ACS Appl. Mater. Interfaces **2023**, *15*, 25, 29655−29673. DOI: 10.1021/acsami.3c02507

Cite This: https://doi.org/10.1021/acsami.4c08962

Read Online

ACCESS | Metrics & More | Article Recommendations

In the original version of this article, the reference numbers in Tables 2, 3, and 4 are wrong. The correct tables are listed below.

Also the original Acknowledgment section has a mistake, in which the INL support should be removed since the writing of this review was finished before and without the INL support. The correct Acknowledgment should read as follows: T.F. and H.Z. acknowledge the support from the University of Utah and the ORAU Ralph E. Powe Junior Faculty Enhancement Award. Z.C. acknowledges the Fundamental Research Funds for the Central Universities, Peking University.

Downloaded via UNIV OF UTAH on June 25, 2024 at 16:03:48 (UTC).
See https://pubs.acs.org/sharingguidelines for options on how to legitimately share published articles.

ACS Publications © XXXX American Chemical Society

Table 2. Thermal Boundary Conductance between GaN and Other Materials[a]

	Growth Method	Interlayer	Measurement Method	TBC (MW m^{-2} K^{-1})	Ref.
GaN/diamond	CVD	None	TTR	4.5	Waller 2020 [84]
GaN/diamond	CVD	None	CTR	12–15	Gu 2016 [52]
GaN/diamond	CVD	None	TDTR	21.2	Yates 2018 [85]
GaN/diamond	MBE	Unknown	Optical	<10	Kuzmik 2011 [145]
GaN/diamond	High-T bonding	Adhesion layer	TDTR	21–28	Cho 2013 [108]
GaN/diamond	RT SAB	2nm a-Si+2.2nm a-dia	TDTR	92	Cheng 2020 [104]
GaN/diamond	CVD	~5 nm AlN	CTR	55–100	Gu 2016 [52]
GaN/diamond	CVD	~5 nm SiN_x	TDTR	~100	Yates 2018 [85]
GaN/diamond	CVD	~5 nm SiN_x	TTR	~150	Zhou 2017 [4,86]
GaN/diamond	CVD	~5 nm SiN	CTR	167–400*	Gu 2016 [52]
GaN/diamond	MOCVD	~5 nm SiN_x	TTR	323*	Malakoutian 2021 [53]
GaN/diamond	CVD	~5 nm AlN	TDTR	55	Yates 2018 [85]
GaN/diamond	SAB	10nm a-Si+3nm a-dia	TDTR	53	Cheng 2020 [104]
GaN/diamond	SAB+800°C ann.	15nm c-Si+3nm a-dia	TDTR	70	Mu 2021 [105]
GaN/diamond	SAB	15nm a-Si+3nm a-dia	TDTR	30	Mu 2021 [105]
GaN/diamond	SAB	22nm a-Si+3nm a-dia	TDTR	25	Mu 2021 [105]
GaN/diamond	SAB+800°C ann.	24nm c-Si+3nm a-dia	TDTR	85	Mu 2021 [105]
GaN/diamond	High-T bonding	~22 nm SiN_x	TDTR	51–57	Cho 2017 [109]
GaN/diamond	CVD	~25 nm SiN_x	TDTR	~35	Cho 2014 [87]
GaN/diamond	CVD	~25 nm dielectric	Raman	~37	Pomeroy 2013 [146], 2014 [89]
GaN/diamond	CVD	28 nm SiN_x	TTR	83	Sun 2015 [90]
GaN/diamond	High-T bonding	~31 nm SiN	TDTR	31	Cho 2017 [109]
GaN/diamond	CVD	~40 nm dielectric	Raman	34.5	Altman 2014 [91]
GaN/diamond	CVD	~50 nm dielectric	Raman	56	Dumka 2013 [92]
GaN/diamond	PVD	Ti (5 nm)/AuSn (40 nm)/Ti (5 nm)	TDTR	13.2	Yang 2021 [83]
GaN/diamond	CVD	~50 nm dielectric	Raman	~28	Pomeroy 2014 [89]
GaN/diamond	Simulations	None	NEMD Tersoff	~13	Tao 2017 [147]
GaN/diamond	Simulations	Monolayer graphene	NEMD Tersoff	~15	Tao 2017 [147]
GaN/diamond	Simulations	Trilayer graphene	NEMD Tersoff	~4	Tao 2017 [147]
GaN/diamond	Simulations	Interlaced teeth	NEMD Tersoff	~19	Tao 2017 [147]
GaN/diamond	Simulations	Interlaced teeth w/ monolayer graphene	NEMD Tersoff	~29	Tao 2017 [147]
GaN/diamond	Simulations	Interlaced teeth w/ trilayer graphene	NEMD Tersoff	~14	Tao 2017 [147]
GaN/diamond	AMM	N/A	Theory	~333	Cho 2017 [109]
GaN/SiC	MBE	None	FDTR	230	Ziade 2015 [80]
GaN/SiC	SAB	3 nm a-SiC	TDTR	170	Mu 2019 [106]
GaN/SiC	SAB+1000°C ann.	3 nm c-SiC (inhomo.)	TDTR	230	Mu 2019 [106]
GaN/SiC	CVD	5nm SiN	TTR	154	Zhou 2017 [86]
GaN/SiC	MOCVD	36 nm AlN	TDTR	200	Cho 2012 [78,148]
GaN/SiC	MBE	38 nm AlN	TDTR	185	Cho 2014 [87]
GaN/SiC	Epitaxial growth	50 nm AlN	TTR	40	Liu 2019 [113]
GaN/SiC	PVD	Ti (5 nm)/AuSn (40 nm)/Ti (5 nm)	TDTR	14.8	Yang 2021 [83]
GaN/SiC	MOCVD	Unknown	TIM	8.3	Kuzmík 2007 [149]
GaN/SiC	Simulations	None	NEMD Tersoff	~520	Hu 2011 [150]
GaN/SiC	Simulations	None	NEMD Tersoff	420	Hu 2013 [151]
GaN/SiC	Simulations	None	NEMD Tersoff	470	Lee 2016 [152]
GaN/SiC	Simulations	None	NEMD Tersoff	794	Lee 2017 [153]
GaN/SiC	Simulations	None	NEMD Tersoff	495	Li 2019 [154]
GaN/SiC	Simulations	None	NEMD Tersoff	470	Lee 2018 [155]
GaN/SiC	Simulations	4 nm $Ga^{15}N$ (isotope)	NEMD Tersoff	555	Lee 2018 [155]
GaN/SiC	Simulations	1×8 nm interlaced teeth	NEMD Tersoff	~800	Hu 2011 [150]
GaN/SiC	Simulations	1 nm AlN	NEMD Tersoff	570–630	Hu 2011 [150]
GaN/SiC	Simulations	Graphene	NEMD Tersoff	601	Hu 2013 [151]
GaN/SiC	Simulations	1×5-8 nm teeth	NEMD Tersoff	670	Lee 2016 [152]
GaN/SiC	Simulations	2.6 nm AB (m_A=51.7, m_B=10.3)	NEMD Tersoff	971	Lee 2017 [153]
GaN/SiC	Simulations	2.5 nm 10% boron dop.	NEMD Tersoff	716	Li 2019 [154]
GaN/SiC	Simulations	2.5 nm 50% boron allo.	NEMD Tersoff	755	Li 2019 [154]
GaN/SiC	Simulations	2.5 nm 10% boron allo.	NEMD Tersoff	577	Li 2019 [154]
GaN/Si	MBE	38 nm AlN	TDTR	188*	Cho 2012 [78]
GaN/Si	MBE	38 nm AlN	TDTR	128	Cho 2014 [79]
GaN/Si	MOCVD	100 nm AlN	TDTR	263	Yates 2015 [99]
GaN/Si	PVD	Ti (5 nm)/AuSn (40 nm)/Ti (5 nm)	TDTR	16.5	Yang 2021 [83]
GaN/AlN	MBE	None	TDTR	620	Koh 2009 [156]
GaN/AlN	Simulations	None	EMD/NEMD (SW) extplt. to ∞	~1150–1300	Liang 2014 [157,158]
GaN/AlN	Simulations	None	NEMD (Tersoff)	475	Lee 2018 [155]
GaN/AlN	Simulations	None	Green's function	300	Polanco 2019 [159]
GaN/AlN	Simulations	None	NEMD SW ex. ∞	825	Wang 2021 [160]
GaN/AlN	Simulations	None	NEMD LJ	780	Bao 2022 [161]
GaN/AlN	Simulations	None	Monte Carlo	870	Bao 2022 [161]
GaN/AlN	Simulations	None	NEMD SW	937	Sun 2021 [162]
GaN/AlN	Simulations	None	NEMD (Tersoff – mixing rule)	3124	Sun 2021 [162]
GaN/AlN	Simulations	None	NEMD (Transf. Tersoff)	3225	Sun 2021 [162]
GaN/AlN	Simulations	2 nm amorphous layer	NEMD SW	149	Wang 2021 [160]
GaN/AlN	Simulations	2 nm ann. cryst. layer	NEMD SW	197	Wang 2021 [160]
GaN/AlN	Simulations	Dislocation (lat. mis.)	NEMD SW	496	Sun 2021 [162]
GaN/AlN	Simulations	Dislocation (lat. mis.)	NEMD (Tersoff – mixing rule)	2440	Sun 2021 [162]
GaN/AlN	Simulations	Dislocation (lat. mis.)	NEMD (Transf. Tersoff)	1933	Sun 2021 [162]
GaN/BAs	Oxygen plasma	2-nm amorphous Al_2O_3	TDTR	250	Kang 2021 [101]
GaN/Al_2O_3	MOCVD	Unclear	TDTR	10	Wang 2014 [163]
GaN/Al_2O_3	MOCVD	Unclear	TIM	8.3	Kuzmík 2007 [149]
GaN/Al_2O_3	MOCVD	Unclear	3ω method	10	Wang 2015 [164]
GaN/SiO_2	Plasma-enh. CVD	Unclear	3ω method	15	Wang 2015 [164]
GaN/ZnO	PVD	10–12 nm defective	TDTR	490	Gaskins 2018 [165]
GaN/ZnO	Model	None	DMM	240	Gaskins 2018 [165]
GaN/ZnO	Simulations	None	AGF DFT	295	Gaskins 2018 [165]
GaN/Al	PVD	Unclear	TTR	190	Stevens 2005 [114]
GaN/Al	PVD	Unclear	TDTR	92	Donovan 2014 [12]
GaN/Al	PVD	Unclear	TDTR	160	Wang 2014 [163]
GaN/Al	PVD	Unclear	TDTR	47–161	Cho 2014 [79]
GaN/Al	PVD	Unclear	TDTR	400	Koh 2021 [81]
GaN/Au	PVD	Unclear	TDTR	55	Donovan 2014 [12]
GaN/Au	PVD	Ti adhesion layer	TDTR	~250	Donovan 2014 [12]
GaN/Cr	PVD	Unclear	TTR	230	Stevens 2005 [114]
GaN/Au or Cr	PVD	Unclear	FDTR	180	Freedman 2013 [166]
GaN/Al	Simulations	None	NEMD LJ	211	Jones 2013 [167]
GaN/Al	Simulations	Al-Ga contact	NEMD SW	99	Zhou 2013 [168]
GaN/Al	Simulations	3×7 nm Al-Ga teeth	NEMD SW	102	Zhou 2013 [168]
GaN/Al	Simulations	3×7 nm Al-N teeth	NEMD SW	172	Zhou 2013 [168]
GaN/Al	NE Landauer	None	DFT	427	Koh 2021 [81]

[a]Greened and greyed boxes are for experimental and simulation data, respectively. *These values may have a large uncertainty.

Table 3. Thermal Boundary Conductance of Si/Diamond and Si/SiC Interfaces

	Growth/ Simulation Method	Interlayer	Measurement Method/Interatomic Potential	TBC (MW m^{-2} K^{-1})	Ref.
Si/diamond	Graphoepitaxy	None	TDTR	64	Cheng 2019 [76]
Si/diamond	CVD	None	TPS	50-100	Goyal 2010 [94]
Si/diamond	Unclear	Unclear	Unclear	30	Goodson 1994 [172]
Si/diamond	CVD	~10 nm amorph.	Joule-heating	>67	Goodson 1995 [96]
Si/diamond	CVD	Unclear	Laser pulse	18	Klokov 2010 [97]
Si/diamond	CVD	Unclear	3ω method	50	Mohr 2017 [98]
Si/diamond	Graphoepitaxy	47×69 nm teeth	TDTR	105	Cheng 2019 [76]
Si/diamond	Graphoepitaxy	105×210 nm teeth	TDTR	80	Cheng 2019 [76]
Si/diamond	Simulations	None	NEMD Tersoff (45nm)	381	Cheng 2019 [76]
Si/diamond	Simulations	2 nm a-C	NEMD Tersoff (45nm)	378	Cheng 2019 [76]
Si/diamond	Simulations	None	NEMD Brenner (6nm)	238	Khosravian 2013 [173]
Si/diamond	Simulations	None	NEMD Brenner (13nm)	482	Khosravian 2013 [173]
Si/SiC	Low-temp. CVD	None	TDTR	600	Cheng 2022 [174]
Si/SiC	Hydrophobic bonding	0.2–2.5nm a-SiO_2	TTR	100–250	Field 2022 [102]
Si/SiC	Hydrophilic bonding	2.5 nm a-SiO_2	TTR	80–110	Field 2022 [102]
Si/SiC	NEMD	None	Tersoff	890	Xu 2022 [77]
Si/SiC	NEMD	Interlaced teeth	Tersoff	300–1000	Xu 2022 [77]

Table 4. Thermal Boundary Conductance between β-Ga_2O_3 and Other Materials

β-Ga_2O_3/substrate	Growth/Simulation Method	Interlayer	Method	TBC (MW m^{-2} K^{-1})	Ref.
Ga_2O_3/diamond	Transferred	None (van der Waals)	TDTR	17	Cheng 2019 [66]
Ga_2O_3/diamond	ALD	None (ultra-clean)	TDTR	179	Cheng 2019 [66]
Ga_2O_3/diamond	ALD	Ga-rich	TDTR	136	Cheng 2019 [66]
Ga_2O_3/diamond	ALD	O-rich	TDTR	139	Cheng 2019 [66]
Ga_2O_3/diamond	Hydrophilic bonding + 250 °C annealing	None (ultra-clean)	-	-	Matsumae 2020 [103]
Ga_2O_3/SiC	SAB + 800 °C ann.	Unclear	TDTR	150	Cheng 2021 [175]
Ga_2O_3/SiC	SAB	30nm Al_2O_3 + 3.5nm a-SiC	TDTR	72	Cheng 2020 [61]
Ga_2O_3/SiC	SAB + 800 °C ann.	30nm Al_2O_3 + 2nm a-SiC	TDTR	65	Cheng 2020 [61]
Ga_2O_3/SiC	SAB	9.4nm Al_2O_3 + 2.7nm a-SiC	TDTR	100	Cheng 2020 [61]
Ga_2O_3/SiC	SAB + 800 °C ann.	9nm Al_2O_3 + 2nm a-SiC	TDTR	88	Cheng 2020 [61]
Ga_2O_3/SiC	SAB	1.8nm a-Ga_2O_3 + 2.2nm a-SiC	-	-	Xu 2019 [107]
Ga_2O_3/SiC	SAB + 1000 °C ann.	1.5nm crystal defective layer	TDTR	244	Liang 2022 [176]
Ga_2O_3/SiC	SAB + 200 °C ann.	1.3nm a-Ga_2O_3 + 2.2nm a-SiC	-	-	Xu 2019 [107]
Ga_2O_3/diamond	Theory	None	DMM	312	Cheng 2019 [66]
Ga_2O_3/Au	Wedge deposition	None	FDTR	45	Aller 2019 [177]
Ga_2O_3/Au	E-beam evaporation	Defective layer	TDTR	31.2	Shi 2021 [63]
Ga_2O_3/Ti	E-beam evaporation	Defective layer	TDTR	17.4	Shi 2021 [63]
Ga_2O_3/Ni	E-beam evaporation	Defective layer	TDTR	82.7	Shi 2021 [63]
Ga_2O_3/Al	E-beam evaporation	Defective layer	TDTR	81.7	Shi 2021 [63]
Ga_2O_3/Au	Wedge deposition	2.5 nm Cr	FDTR	530	Aller 2019 [177]
Ga_2O_3/Au	Wedge deposition	5 nm Ti	FDTR	260	Aller 2019 [177]
Ga_2O_3/Au	Wedge deposition	>3 nm Ni	FDTR	410	Aller 2019 [177]
Ga_2O_3/Au	Theory	None	DMM	71.2	Shi 2021 [63]
Ga_2O_3/Ti	Theory	None	DMM	103	Shi 2021 [63]
Ga_2O_3/Ni	Theory	None	DMM	126	Shi 2021 [63]
Ga_2O_3/Al	Theory	None	DMM	139.6	Shi 2021 [63]
Ga_2O_3/Cr	Theory	None	DMM	148.7	Shi 2021 [63]

https://doi.org/10.1021/acsami.4c08962
ACS Appl. Mater. Interfaces XXXX, XXX, XXX−XXX